



Article

Multi-Sensor Retrieval of Aerosol Optical Properties for Near-Real-Time Applications Using the Metop Series of Satellites: Concept, Detailed Description, and First Validation

Michael Grzegorski, Gabriele Poli , Alessandra Cacciari, Soheila Jafariserajehlou, Andriy Holdak, Ruediger Lang, Margarita Vazquez-Navarro, Rosemary Munro and Bertrand Fougnie *

EUMETSAT, Eumetsat Allee 1, 64295 Darmstadt, Germany; Michael.Grzegorski@external.eumetsat.int (M.G.); Gabriele.Poli@external.eumetsat.int (G.P.); Alessandra.Cacciari@eumetsat.int (A.C.); Soheila.Jafariserajehlou@external.eumetsat.int (S.J.); Andriy.Holdak@external.eumetsat.int (A.H.); Ruediger.Lang@eumetsat.int (R.L.); Margarita.Vazquez@eumetsat.int (M.V.-N.); Rosemary.Munro@eumetsat.int (R.M.)

* Correspondence: Bertrand.Fougnie@eumetsat.int

Abstract: The Polar Multi-Sensor Aerosol product (PMAp) is based on the synergistic use of three instruments from the Metop platform, GOME-2, AVHRR, and IASI. The retrieval algorithm includes three major steps: a pre-identification of the aerosol class, a selection of the aerosol model, and a calculation of the Aerosol Optical Depth (AOD). This paper provides a detailed description of the PMAp retrieval, which combines information provided by the three instruments. The retrieved AOD is qualitatively evaluated, and a good temporal as well as spatial performance is observed, including for the transition between ocean and land. More quantitatively, the performance is evaluated by comparison to AERONET in situ measurements. Very good consistency is also observed when compared to other space-based data such as MODIS or VIIRS. The paper demonstrates the ability of this first generation of synergistic products to derive reliable AOD, opening the door for the development of synergistic products from the instruments to be embarked on the coming Metop Second Generation platform. PMAp has been operationally distributed in near-real-time since 2014 over ocean, and 2016 over land.

Keywords: remote sensing; aerosol optical depth; synergy; Metop; GOME-2



Citation: Grzegorski, M.; Poli, G.; Cacciari, A.; Jafariserajehlou, S.; Holdak, A.; Lang, R.; Vazquez-Navarro, M.; Munro, R.; Fougnie, B. Multi-Sensor Retrieval of Aerosol Optical Properties for Near-Real-Time Applications Using the Metop Series of Satellites: Concept, Detailed Description, and First Validation. *Remote Sens.* **2022**, *14*, 85. <https://doi.org/10.3390/rs14010085>

Academic Editor: Yolanda Sola

Received: 27 October 2021

Accepted: 21 December 2021

Published: 24 December 2021

Publisher's Note: MDPI stays neutral with regard to jurisdictional claims in published maps and institutional affiliations.



Copyright: © 2021 by the authors. Licensee MDPI, Basel, Switzerland. This article is an open access article distributed under the terms and conditions of the Creative Commons Attribution (CC BY) license (<https://creativecommons.org/licenses/by/4.0/>).

1. Introduction

Aerosols are solid or liquid particles suspended in the Earth's atmosphere transported over short to large distances. This definition comprises various types of particles with different sources and shapes, as well as different physical properties and chemical compositions. Atmospheric aerosols affect air quality, which, in turn, affects human health and the overall ecosystem. Because aerosols have direct and indirect radiative effects, they play an important role in the Earth's radiation budget and, therefore, in the overall climate system [1]. Aerosols are, therefore, very relevant to policy issues in both air quality and climate sciences. In fact, air pollution by particulate matter (PM) is probably the most pressing issue in air quality regulation worldwide, and, at the same time, it represents one of the biggest sources of uncertainties in current climate simulations [1,2].

In order to understand the role of aerosols in the atmosphere and in the overall climate system, observations of aerosol properties and of their spatiotemporal distribution and abundance are needed. In addition, aerosol parameters are required as input for atmospheric and Earth-system models in order to provide forecasts of global aerosol distribution—and in particular of critical events such as volcanic eruptions, dust-storms or other major pollution events—as well as for the modeling of past and future climate systems [3,4].

Satellite-based observations can provide a wide range of parameters describing aerosol properties at a global scale and for various time scales. Many applications require the provision of aerosol data in near-real-time (NRT), i.e., provided “on-line” within minutes to hours after the sensing time, with a high degree of reliability and availability. NRT data are needed for Air Quality, Numerical Weather Prediction, National Meteorological Services, and Advisory Centers for sand, dust, and volcanic ash. Other applications, such as the provision of climate data records, are not demanding in terms of timeliness, and aerosol data can be provided “off-line.”

Since aerosols are the product of a large variety of natural and anthropogenic processes, they form highly variable mixtures of different chemical and microphysical compositions and abundance, which make their quantitative characterization very difficult, in particular when using remote sensing techniques. The intrinsic complexity of aerosols, therefore, requires the combination of observations covering a large spectral range at moderate spectral resolution from the ultraviolet (UV) to the thermal infra-red (TIR). In addition to the spectral information, the scattering properties of aerosols can be assessed through observations of a range of scattering angles, especially when this is combined with polarized measurements. Ideally, high spatial and temporal resolution observations are needed to disentangle the aerosol from the surface signal better and address the diurnal variation of the aerosol load. Up to now, no single space-based instrument is capable of providing such a combination of measurements.

To date, the highest information content on aerosol properties derived from a single space-based instrument has been provided by multi-angular polarimeters in the visible to the near-infrared range [5,6], such as by the various POLDER missions [7–9]. POLDER not only allowed the retrieval of the aerosol optical depth (AOD) but was also able to characterize other aerosol optical and microphysical properties, such as single-scattering albedo (SSA), refractive index (real and imaginary parts), particle size distribution, and, with some limitation, aerosol height. Because the information content is high, the POLDER multi-angular observations also allowed the simultaneous retrieval of both surface and aerosol properties [10,11].

In contrast, the (A)ATSR series of instruments on the European satellites ERS, ERS-2, and ENVISAT and the MODIS instruments on NASA’s Terra and Aura platform have thus far been delivering the largest data-sets, about 20 years of data, of aerosol products over land at high spatial coverage and accuracy.

The (A)ATSR instruments measure at two different viewing angles for 11 spectral bands from visible to TIR. However, only four of these bands are available in the reflective spectral-domain useful for aerosol retrieval. The dual-view observations are essential for the separation of the surface and aerosol scattering contributions to the measured signal at the top of the atmosphere [12]. The (A)ATSR instruments have been used to produce aerosol climatologies within the European Climate Change Initiative (CCI) [13]. A multi-instrument approach combining AATSR with an optical spectrometer has also been developed [14]. A long time series from 1995 to 2012 has been retrieved within the CCI, but newer data are not available due to ENVISATs end-of-lifetime in 2012. Since 2016, a new time series of AOD retrieved from a dual-view instrument has started with SLSTR on Sentinel-3A and 3B [15].

The MODIS instruments provide observations in 36 spectral bands ranging from 0.4 μm to 14.4 μm for a single view. The MODIS instrument is considered as a reference for AOD retrieval from space due to its extensive validation and its long time series started in 1999. The primary MODIS aerosol retrieval makes use of the dark target approach [16] with restrictions to areas where the contribution of the surface reflectance is moderately small. This approach does not provide results over bright surfaces such as deserts because the uncertainties on the a priori surface reflection increase or because the amount of light reflected by aerosol as compared to the surface becomes unfavorable (see, for instance, the critical surface albedo [17]). To better handle these types of surfaces, it is necessary to use shorter wavelengths, typically below 0.5 μm , for which the surface contribution is smaller. This

was implemented in the MODIS retrieval in the deep-blue algorithm [18,19]. The deep-blue algorithm is currently used in combination with the dark target approach [20] to provide global aerosol information, also over bright surfaces such as deserts. Other more recent approaches also try to simultaneously retrieve the surface and aerosol from the time series of observations [21,22]. Note that the MISR instrument on the Terra platform, providing observations for nine viewing directions and four spectral bands, is also contributing to an observational dataset of aerosol properties for more than 20 years.

For all aerosol retrievals, including the ones mentioned thus far, the a priori knowledge on the presence of clouds and the subsequent differentiation between cloud and aerosol remains a critical issue. Even if *a posteriori* filtering is still possible (e.g., based on goodness-of-fit [23]), most of the aerosol retrievals are conducted when the pixel is primarily declared cloud-free. This cloud masking should be defined sufficiently robustly such that pixels in the vicinity of clouds (up to a couple of kilometers depending on cloud and atmosphere properties), which are cloud-affected, are also discarded. Sub-pixel clouds are also challenging. If not detected, they may be assigned to aerosol by the retrieval. Only observations with a higher spatial resolution allow the detection of sub-pixel clouds and potentially some decontamination. Aerosol retrieval can also be conducted when the pixel is cloudy. For example, aerosol plumes above clouds can be detected using polarization [24] or thermal infrared observations [25].

A challenging part of an aerosol retrieval algorithm is to properly disentangle the surface and aerosol contributions to the measured Top-of-Atmosphere (TOA) signal. In many situations, the spectral and/or directional signature can be used in addition to a priori assumptions on the surface contribution. As for cloud detection, sub-pixel information from a higher spatial resolution instrument would also provide very valuable information for better characterization of the heterogeneity of the surface or the target in general. The Polar Multi-Sensor Aerosol Product (PMAp) is based on a multi-instrument approach from sensors of a single polar platform, Metop from the EUMETSAT Polar System (EPS) [26]. Measurements available on the Metop platform are combined to form a “hyper-instrument” providing a very rich spectral coverage from the Ultra-Violet to the Thermal Infrared, the measurement of polarization, and multi-resolution spatial information. For this, PMAp exploits the synergy of observations coming from the 2nd Global Ozone Monitoring Experiment (GOME-2), the Advanced Very-High Resolution Radiometer (AVHRR), and the Infra-red Atmospheric Sounding Interferometer (IASI), to derive the Aerosol Optical Depth (AOD) at 550 nm at the spatial resolution of the 10 km × 40 km (Metop-B and -C) and 5 km × 40 km (Metop-A). Additional information is also provided on the aerosol class. PMAp version 1 was introduced operationally in the EUMETSAT ground segment in February 2014, providing NRT aerosol optical properties over ocean surfaces only. Since February 2016, the PMAp version 2 products provided global aerosol data (including land surface). PMAp data are available on average 1.5 h after sensing via EUMETSAT’s EUMETCast near-real-time distribution system [27,28].

2. Multi-Instrument Single-Platform Concept for Aerosol Retrieval

2.1. The PMAp Approach

PMAp makes use of measurements by GOME-2, AVHRR/3, and IASI, with the GOME-2 footprint as its co-registration target. PMAp uses the GOME-2 polarization measurement devices (PMDs), which provide, in addition to its hyper-spectral main channels, measurements of un-polarized and polarized reflectance (the Stokes fraction Q/I) [29]. The spatial resolution of the PMD observations, which is also the resolution of the PMAp level-2 products, is 10 × 40 km² for Metop-B and -C, and 5 × 40 km² for Metop-A. AVHRR/3 is a scanning radiometer successfully used to retrieve AOD over the sea from the NOAA satellite platforms [30], and algorithms not in operational use also exist over some types of land surface [31–33]. GOME-2 and AVHRR/3 have complementary spectral ranges, which provide coverage from the Ultra-violet to the Thermal infrared, overlapping in the visible spectral range. The difference in their spatial resolutions is also an important asset. The

observational capabilities of AVHRR/3 at $1 \times 1 \text{ km}^2$ spatial resolution are mainly exploited for accurate cloud masking and cloud correction (or decontamination) together with the evaluation of the scene homogeneity inside the rather large GOME-2 footprint. Finally, the spectra provided by the IASI thermal infrared spectrometer [34] at very high spectral resolution add significant information to the retrieval with respect to the detection of desert dust and volcanic ash [25].

The PMAp development has two important features. First, PMAp makes use of the fully operational EUMETSAT infrastructure, with all EPS data processed on a single ground segment, providing an operational aerosol product based on data acquired on the EPS morning orbit (9:30 equatorial crossing time) and disseminated in near-real-time to operational users. PMAp, therefore, provides AOD information in addition to aerosol class and other relevant parameters (e.g., cloud fraction, chlorophyll concentration, etc.) in near-real-time for direct assimilation, e.g., by the Copernicus Atmosphere Monitoring Service forecast system, in addition to the already assimilated MODIS data [35]. Second, PMAp serves as proof-of-concept for an operational aerosol product derived from the combination of multiple sensors requiring, as a prerequisite, a multi-sensor co-registration framework. This framework is currently being extended to a multi-sensor retrieval framework for the retrieval of aerosol properties from EPS-SG, combining observations from the 3MI polarimeter, the VII cloud imager, and the IASI-NG and Sentinel-5 spectrometers [36]. The lifetime of the EPS mission serving PMAp spans from 2006 to 2027 and beyond, and the follow-on EPS-SG mission is planned to be operational in the 2024 to 2046 timeframe.

2.2. Sensors Contributing to PMAp

2.2.1. The Global Ozone Monitoring Experiment (GOME-2)

GOME-2 is an optical spectrometer fed by a scan mirror, which enables across-track scanning in nadir, as well as sideways viewing for polar coverage and instrument characterization measurements using the moon [29,37]. GOME-2 senses the Earth's backscattered radiance and extraterrestrial solar irradiance in the ultraviolet and visible part of the spectrum (240–790 nm) at a high spectral resolution of 0.26–0.51 nm. The instrument comprises four main optical channels, which focus the spectrum on linear detector arrays of 1024 pixels each, and two polarization measurement devices (PMDs) containing the same type of arrays for measurement of linearly polarized intensity in two perpendicular directions (called PMD-S and PMD-P). The definition of the bands is provided in Munro et al. [29], and the associated mean values are reported in Table 1. The PMDs are required because GOME-2 is a polarization-sensitive instrument. The PMD measurements are performed at the lower spectral resolution but at higher spatial resolution than the main science channels. The PMD-S and PMD-P bands are combined to derive the un-polarized TOA reflectance and its polarized component, the Stokes fraction q defined by Q/I . Both un-polarized and polarized reflectances were used for 11 of the 15 spectral bands covering the region from 312 to 800 nm (Table 1). The corresponding PMD footprint was 10 km across-track \times 40 km along-track for a nominal swath width of 1920 km. Metop-A is operated in a different mode with a reduced swath of 960 km (from July 2013) and an increased spatial resolution of the PMDs ($5 \times 40 \text{ km}^2$). The PMDs also facilitate sub-pixel determination of cloud fraction [38] at a higher spatial resolution than the operational cloud retrieval applied to the main science channels [39]. In addition, AVHRR based cloud coverage and cloud inhomogeneity within a GOME-2 pixel is delivered by EUMETSAT operationally together with the spectra in the GOME-2 Level-1 product.

Table 1. Band definition for the EPS instruments contributing to the spectral synergy used in PMAp and sorted by increasing wavelength. PMD bands from GOME2 with their central wavelength (CWL in μm) and full width half maximum (FWHM in μm). Values are an average of PMD-S and PMD-P bands [29]. Only PMD-4 to PMD-14 are used in PMAp. Spectral Characteristics of AVHRR with their CWL and FWHM. IASI main spectra feature with min-max wavelengths and wave numbers (in cm^{-1}).

| Sensor | Channel | CWL (μm) | FWHM (μm) | Wavelength (μm) | Wave Number (cm^{-1}) |
|--------|---------|-----------------------|------------------------|------------------------------|----------------------------------|
| GOME2 | PMD-4 | 0.3381 | 0.0041 | | |
| GOME2 | PMD-5 | 0.3694 | 0.0171 | | |
| GOME2 | PMD-6 | 0.3821 | 0.0035 | | |
| GOME2 | PMD-7 | 0.4143 | 0.0291 | | |
| GOME2 | PMD-8 | 0.4633 | 0.0578 | | |
| GOME2 | PMD-9 | 0.5220 | 0.0539 | | |
| GOME2 | PMD-10 | 0.5546 | 0.0037 | | |
| GOME2 | PMD-11 | 0.5908 | 0.0449 | | |
| AVHRR | 1 | 0.630 | 0.100 | | |
| GOME2 | PMD-12 | 0.6403 | 0.0441 | | |
| GOME2 | PMD-13 | 0.7568 | 0.0241 | | |
| GOME2 | PMD-14 | 0.7992 | 0.0089 | | |
| AVHRR | 2 | 0.865 | 0.275 | | |
| AVHRR | 3a | 1.610 | 0.060 | | |
| IASI | 3 | | | 3.62–5.00 | 2000.0–2760.0 |
| AVHRR | 3b | 3.740 | 0.380 | | |
| IASI | 2 | | | 5.00–8.26 | 1210.0–2000.0 |
| AVHRR | 4 | 10.800 | 1.000 | | |
| AVHRR | 5 | 12.000 | 1.000 | | |
| IASI | 1 | | | 8.26–15.50 | 645.0–1210.0 |

Instrument degradation has been observed in GOME-2, causing a differential spectral degradation (different for radiance and solar irradiance) in the measured signals, which could affect the retrieval of several L2 products. As the degradation is spectrally inhomogeneous, it has the potential to impact the aerosol optical properties retrieval significantly. Potential contributors to the observed signal degradation of GOME-2 were identified as internal contamination of the optical path, degradation of the scan mirror with viewing angle-dependent response, and solar optical path degradation. In addition, the thermal instability of the optical bench contributes to spectral instability. A model of this degradation was developed taking into account the above-mentioned issues, and a platform-dependent matrix of time-dependent spectral coefficients was computed to correct the PMD channel signals [29]. This correction, derived for each GOME-2 instrument on the 3 Metop platforms, was now in use in PMAp. Figure 3, also described in Section 2.4, illustrates the improvement in the Level-1C reflectance when the degradation correction is applied to the Level-1B data, resulting in a much better correlation with AVHRR reflectance.

Note that a radiometric adjustment of the PMD reflectance was also introduced for the bands used to derive the AOD (bands 7, 8, and 12). A significant difference was detected between the TOA reflectance and reflectances calculated for conditions, which maximize the contribution of Rayleigh scattering, thereby increasing the relevance of the comparison. For bands 7 and 8, measurements were collected over dark surfaces, and after the rejection of atmospheric turbidity (using polarization), a radiometric offset was detected. The same was performed for band 12 over the ocean. It is not the goal of this paper to detail this radiometric adjustment, but more details can be found in [40].

2.2.2. The Advanced Very High-Resolution Radiometer (AVHRR/3)

AVHRR/3, hereafter called AVHRR, is a six-channel scanning radiometer equipped with three solar channels in the visible and short-wave infra-red region and three thermal infrared channels. The spectral features of AVHRR are presented in Table 1. AVHRR is an across-track scanning system with a scan range of $\pm 55.37^\circ$ and an instantaneous field of view size of 1.08 km at nadir. The spectral channels of AVHRR/3 are not exactly the same as those of AVHRR/2, and include an additional 3a/b split-window channel. Channel 3a operates in the solar spectral region (1.6 μm) and is available in the daytime, while channel 3b operates in the infrared (3.7 μm) and cannot be used for aerosol retrievals since it is available on the night-side only [41,42].

2.2.3. The Infrared Atmospheric Sounding Interferometer (IASI)

The Infrared Atmospheric Sounding Interferometer (IASI) is a Fourier transform spectrometer, which provides infrared spectra at high spectral resolution (FWMH: 0.5 cm^{-1}) between 645 and 2760 cm^{-1} (3.6 to 15.5 μm) for a spatial resolution of 12 km over a swath of about 2200 km. The main goal of the IASI mission is to provide atmospheric emission spectra for the derivation of temperature and humidity profiles with high vertical resolution and accuracy. Additionally, it is used for the determination of trace gases such as ozone, methane, carbon dioxide, and nitrous oxide, as well as land and sea surface temperature, and emissivity, and cloud properties. IASI is equipped with 8461 spectral channels, aligned in three bands, with a spectral resolution of 0.5 cm^{-1} (FWMH) after apodization (L1c spectra). The spectral sampling interval is 0.25 cm^{-1} . The main spectral features of IASI are reported in Table 1.

2.3. The Colocation Algorithm

A dedicated and computationally efficient algorithm was developed for the colocation of AVHRR and IASI measurements to the corresponding GOME-2 observation in order to allow their synergistic use for NRT aerosol retrieval. This multi-sensor colocation strategy was developed taking into account the exact size and shape of the footprints of the different instruments (Table 2), as well as their projection on the Earth surface, which depends on the viewing geometry.

Table 2. Size and shape of the footprints considered by the colocation algorithm developed for PMAp. ACT and ALT refer to across-track and along-track, respectively.

| Sensor | IFOV Size [km] | | | | IFOV Shape |
|-------------------------|----------------|------|------|------|---------------------|
| | Nadir | | Edge | | |
| | ACT | ALT | ACT | ALT | |
| GOME-2 PMD (Metop A) | 5 | 40 | 10 | 60 | rectangular |
| GOME-2 PMD (Metop B, C) | 10 | 40 | 20 | 60 | rectangular |
| AVHRR (Metop A, B, C) | 1.08 | 1.08 | 6.15 | 2.27 | rectangular |
| IASI (Metop A, B, C) | 12 | 12 | 39 | 20 | circular/elliptical |

The GOME-2 PMD pixel footprint is chosen as the target for the colocation of AVHRR and IASI measurements since the inversion algorithm uses IASI and AVHRR measurements for scene and aerosol type characterization, while the retrieval of AOD is carried out using the GOME-2 PMD reflectances (see Section 3). The algorithm identifies all AVHRR ground pixels within the exact PMD footprint and calculates the percentage of overlap between GOME-2 PMD rectangular and IASI elliptical pixels. Hence, GOME-2 can be referred to as the primary instrument, whereas AVHRR and IASI are the secondary instruments [43] requiring two different steps for the colocation (see hereafter). All three instruments observe the same scene at the same time. The colocation algorithm only focuses on the

geometrical colocations of the footprints in order to ensure that a sufficient number of secondary measurements fully covering the primary area will always be available.

2.3.1. AVHRR/GOME-2 Colocation

The colocation algorithm for AVHRR is based on a technique similar to the “quasi-elliptical approach” described in [43], with the difference that the primary footprint is not elliptical but rectangular. With respect to the GOME-2 footprints, AVHRR pixels are treated as dimensionless points. For this purpose, an accurate Point-in-Polygon approach is applied. A slice of the Earth sphere (locally approximating the ellipsoid) is associated with each GOME-2 footprint, as shown in Figure 1. This shape is called the geoslice and consists of a spherical sector whose spherical cap is a polygon, instead of a circle. In an Earth-fixed Cartesian reference frame with P being the center of an AVHRR footprint, the colocation algorithm analytically evaluates the position of P with respect to the planes delimiting the geoslice (Figure 1).

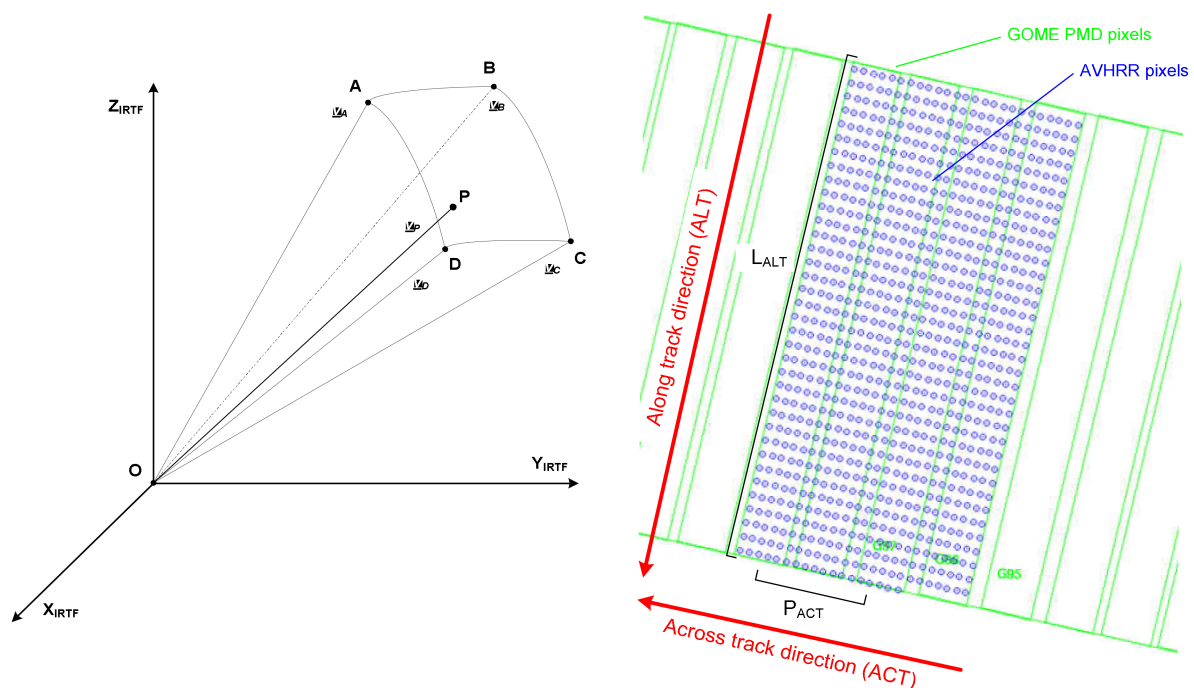


Figure 1. Reference geometry for the “Point-in-Polygon” algorithm in an Earth-fixed reference frame and results of AVHRR/GOME-2 colocation (for Metop-A). (Left), an illustration of the geoslice where ABCD shows a GOME-2 pixel projected on the Earth, and P an AVHRR pixel collocated in this GOME2 pixel. (Right), a result after colocation of all the AVHRR pixels into GOME2 pixels.

For such an approach, the most time-consuming task is the search among the many AVHRR pixels that can potentially be collocated to the GOME-2 pixel (up to 650 AVHRR pixels can be collocated within one of the 192 PMD pixels of a GOME-2 forward scan). The search problem is mitigated by the use of a pivot pixel technique (similar to the one described in [44]). As a consequence, a “brute-force” search among the various AVHRR pixels is only performed for the first GOME-2 pixel of the first GOME-2 scan. Then, for the next GOME-2 footprint, the colocation results of the previous pixel are used to limit the AVHRR search area, thus speeding up the search for the next pixels. For each GOME-2 PMD pixel, the result of the colocation is an array of collocated AVHRR pixels, each of them identified by a scan index and a pixel index along the scan.

The colocation of AVHRR observations into the GOME-2 PMD footprint is fundamentally similar to the one developed for the colocation of VII observations into the 3MI footprint in the context of the EPS-SG mission [45].

2.3.2. IASI/GOME-2 Colocation

The IASI footprint size is comparable to that of the GOME-2 PMD footprint (Table 2), although of a completely different shape. Therefore, IASI pixels cannot be considered dimensionless points. The colocation approach developed for IASI is, therefore, based on a Polygon-Polygon intersection algorithm, which represents both GOME-2 and IASI footprints as two-dimensional convex polygons and aims at calculating the percentage of overlap between them.

As for the AVHRR colocation, the rectangular GOME-2 footprint is represented by a 4-point polygon on the ellipsoidal Earth surface; the elliptical IASI footprint is also approximated by a polygon, whose number of sides can be variable (for the PMAp case, it has been set to 16). Once a set of approximating points is defined for the two footprints, a planar projection (to a local tangent plane) and a rotation of these points are needed in order to transform the two 3D point sets into two 2D convex polygons (Figure 2). The percentage of a GOME-2 pixel overlapping with an IASI pixel is then evaluated using a convex polygon intersection algorithm [46]. As in the case of AVHRR, this Polygon-Polygon algorithm is also based on the search of IASI pixels. Since the number of IASI pixels per scan is not so large—with 30 samples acquired per scan and 4 footprints per sample, thus resulting in 120 footprints per scan—a brute force search is preferred over a pivot pixel strategy in this case, in order to reduce the complexity of the algorithm design. This choice still allows the required level of performance for the NRT processing to be met.

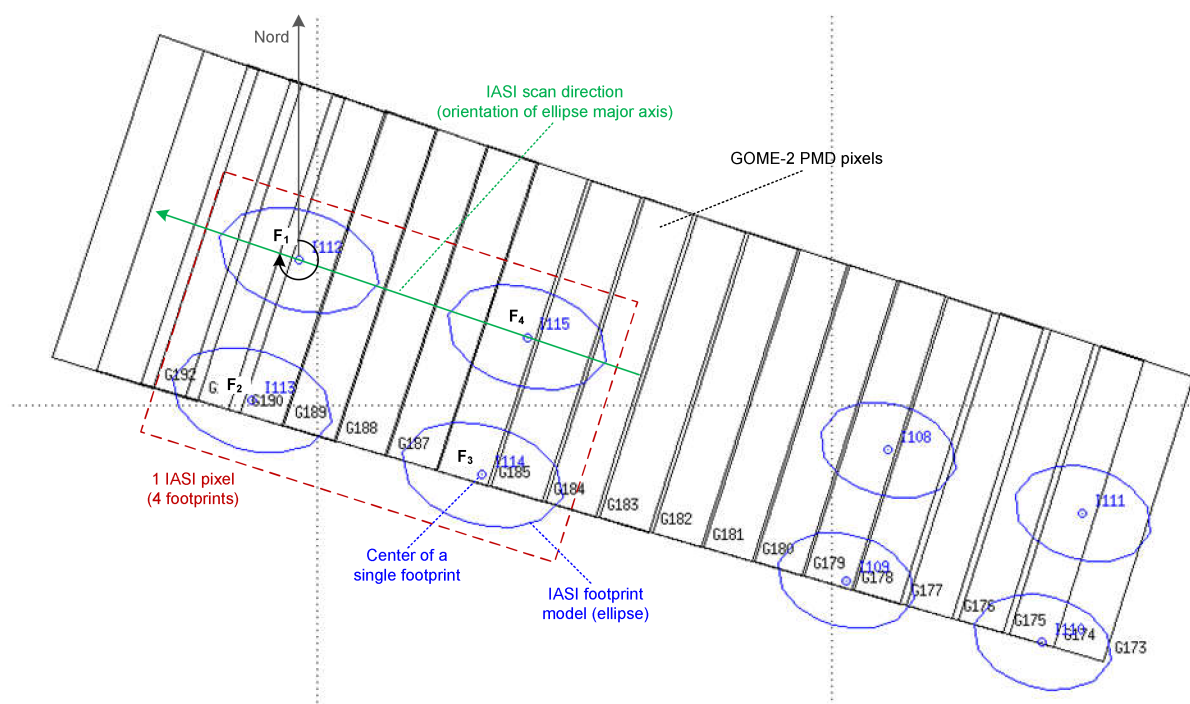


Figure 2. Polygon-Polygon algorithm: results of IASI/GOME-2 colocation (for Metop-A).

For each GOME-2 PMD pixel, the result of the colocation is an array of collocated IASI footprints together with the percentage of the GOME-2 pixel overlapping with them. Again, each IASI footprint is identified by a scan index and a footprint index along the scan.

2.4. Consistency between Co-Registered AVHRR and GOME-2 Information

The reflectance measured in all AVHRR bands and the corresponding cloud mask derived from the AVHRR level-1B product [41,42] is collocated to the GOME-2 PMDs using the point-in-polygon approach described in the previous section. The collocations have to be performed separately for each PMD band because, due to their sequential readout

whilst the scan mirror and satellite are moving, the PMD bands do not cover exactly the same footprint. This effect of non-unique ground pixel footprints within a spectrum is called spatial aliasing and detailed for GOME-2 in Munro et al. [29] and the GOME-2 Factsheet [47]. This type of effect can be critical and is important to consider for the design of the algorithm and its performance, as well as for the estimation of the retrieval error.

The collocation of reflectances measured by AVHRR channel-1, centered at 630 nm, to GOME-2 PMD band 12 at 640 nm is critical for the PMAp algorithm. PMD12 is the band closest in wavelength to AVHRR channel-1. Figure 3 shows the correlation after collocation between AVHRR channel-1 and GOME-2 PMD-12, to which radiometric corrections have been applied (L1C including degradation correction) for one orbit over the Pacific Ocean. A generally good agreement with a very high correlation is found. The discrepancies between the two reflectance data sets, predominantly resulting in a slope different from one, with essentially no offset, are mostly due to a well-known calibration error on AVHRR [48]. Other aspects may also contribute to the absolute calibration error of GOME-2, the slightly different wavelength ranges covered by the two channels, and differences in the shape of their spectral response function, as well as to the error introduced by the collocation algorithm itself. This accuracy is limited by the different shapes of the footprints (elliptical for AVHRR and rectangular for GOME-2), such that the average of all AVHRR pixels within the PMD will not cover exactly the same area on Earth as the PMD. The dispersion observed in Figure 3 is obviously linked to the radiometric inhomogeneity of the pixel, the lower dispersion at very low reflectance being explained by clear sky conditions. The correlation presented in Figure 3 can be used to monitor the potential degradation of the two sensors as well as the efficiency of the collocation process.

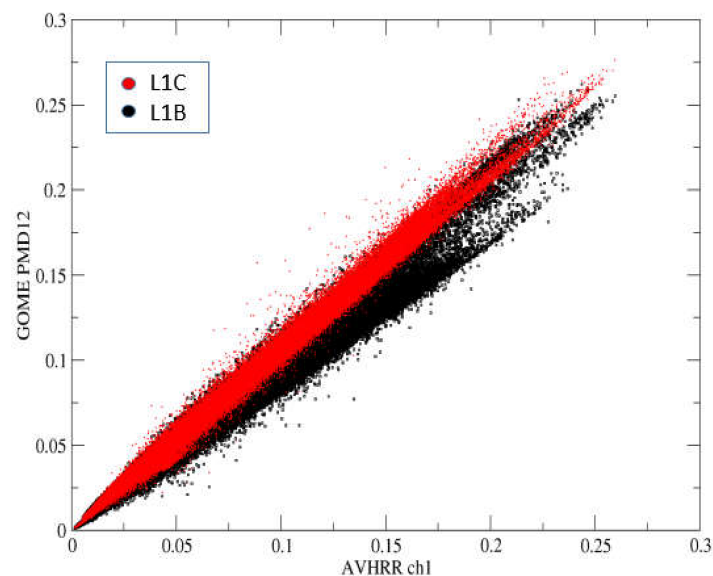


Figure 3. PMD-12 reflectance before (from L1B) and after (from L1C) radiometric correction as a function of collocated AVHRR reflectance in channel 1 for one orbit of acquisition, the 16 October 2017.

3. The PMAp Multi-Sensor Aerosol Retrieval Algorithm

3.1. General Structure

The PMAp algorithm, in order to fulfill the operational NRT requirements, needs to be fast and robust for implementation in EUMETSAT's ground segment. The use of data collected by the three Metop platforms allows for a quasi-daily global coverage since the overpass of every Metop complements the others. The retrieved aerosol maps may contain residual spatial gaps mainly due to cloudy conditions, sun glint, or limitations of the PMAp algorithm (such as for aerosol over bright inhomogeneous surfaces).

Cloud screening is a critical part of every aerosol retrieval approach. Cloudy scenes lead to a significant change in the TOA reflectance as compared to cloud-free scenes,

depending on the cloud type (brightness, opacity, semi-transparency) and surface type (dark or bright). Such cloudy conditions have to be properly masked and/or corrected. The general strategy in PMAp is to use a strict cloud filter at the level of the instrument with the highest spatial resolution (AVHRR) with additional tests enabling the detection of optically thick aerosols, initially detected as clouds. The cloud mask is defined, where possible, as dependent on the aerosol type (see Section 3.3). At the level of the target instrument (GOME-2) with much coarser spatial resolution, the aggregated high spatial resolution cloud mask information is used to correct the reflectances for cloud signals up to a certain level (see Section 3.3.7). This cloud decontamination is an important means to significantly increase the number of retrievals and, as a consequence, the spatial coverage of retrieved AOD.

The GOME-2 PMDs provide unpolarized reflectance and polarization through the Stokes fraction q for the single acquisition viewing geometry. Because the information content of the polarization is largely dependent on the observation angle, the core retrieval, in particular the estimation of the AOD, is based on the unpolarized reflectance, with the Stokes fraction q (i.e., Q/I) being used for fitting other aerosol properties (in the particular aerosol model).

Aerosol retrieval is an under-determined problem, and the best mathematical fit may not always represent the best geophysical solution. During the retrieval of the AOD, the TOA signal is computed and compared to the measured TOA signal considering a series of geophysical parameters such as the aerosol model or the surface type and reflectance. The number of parameters estimated in addition to the AOD has to be realistically adjusted to the information content provided by the sensors. To mitigate this, it is usually needed to include a priori information on some of the input parameters for the calculation of the TOA signal. This approach is also important to provide a level of stability of the algorithm, especially with respect to the changes in the inputs, such as calibration degradation of Level-1 data. An appropriate error characterization suitable for use in data assimilation (see Section 3.4) is also implemented.

Based on these considerations, the PMAp algorithm is structured in three successive steps:

- Step 1 (Multi-Sensor): The multi-sensor part of the retrieval is dedicated to aerosol/cloud discrimination, deriving cloud information, and preliminary classification of the suspended aerosol (through an aerosol class). The result of this step is:
 - A cloud flag to exclude pixels with a large cloud contribution;
 - Cloud decontaminated GOME-2 PMD reflectances for partly cloudy conditions;
 - A flag for thick dust/ash aerosol (also used in Step 2 to constrain the aerosol class);
 - An aerosol class including fine/coarse discrimination;
- Step 2 (GOME-2): For every candidate aerosol model from the aerosol class identified in Step 1, an AOD is derived from the GOME-2 unpolarized reflectance using one single PMD band (the most favorable one: in the red spectral range over the ocean, and in the blue part of the spectrum over land). For cloud-free pixels over the ocean, the surface contribution (parametrised with the chlorophyll concentration) is fitted using the reflectance in two additional bands. The result of this step is:
 - A set of AOD estimates (i.e., one AOD for every candidate aerosol model);
- Step 3 (GOME-2): Reflectance and polarized reflectance from several PMD bands are used in a minimization process to identify the best aerosol model (default aerosol model otherwise). Based on this model, the final AOD is extracted from the set retrieved in step 2. The polarized reflectance (q -Stokes fraction) is used for cloud-free pixels only, and the uncertainty is calculated for the retrieved AOD. The result of this step is:
 - The aerosol model (estimated or default);
 - A final AOD and an estimate of the associated uncertainty;

3.2. Definition of Aerosol Models and Look-Up-Tables

3.2.1. Aerosol LUT

In order to be computationally efficient and at the same time robust, PMAp uses Look up Tables (LUTs) of reflectance and Stokes fraction specifically calculated for GOME-2 spectral bands [49]. Reflectance and Stokes fraction values in the LUTs are functions of the observation geometry, the surface characteristic (albedo), the AOD, and the aerosol type. Table 3 details the microphysical properties of every aerosol model used to generate the PMAp LUTs. All aerosol models are identified by their aerosol Id ranking from 1 to 9.

Table 3. Aerosol micro-physical properties are currently embedded in PMAp, according to Hasekamp et al. [50]. The aerosol Id from 1 to 9, the effective radius (in μm) for the small (fine) and large (coarse) parts, the associated effective variance (in μm), the fraction f_l of large particles, the real n_r and imaginary n_i parts of the refractive index (values are provided at 414 nm and 640 nm when spectrally variable), the aerosol type, the altitude of the layer assumed to be homogeneous, and the surface type for which the aerosol Id is considered.

| Aerosol Id | Effective Radius (μm) | | Effective Variance (μm) | | f_l | Refractive Index | | Aerosol Type | Altitude | Surface Type | Comment |
|------------|------------------------------------|-------|--------------------------------------|-------|------------------|------------------|---------------------------------|--------------|----------|--------------|---------------|
| | small | large | small | large | | n_r | n_i | | | | |
| 1 | 0.11 | 0.84 | 0.65 | 0.65 | $1.53\text{e}-2$ | 1.40 | $-5.0\text{e}-8$ | oceanic | 0–2 km | ocean | |
| 2 | 0.12 | 2.19 | 0.18 | 0.81 | $4.36\text{e}-4$ | 1.40 | $-4.0\text{e}-3$ | industrial | 0–2 km | land/ocean | |
| 3 | 0.14 | 2.15 | 0.22 | 0.62 | $7.00\text{e}-4$ | 1.45 | $-1.2\text{e}-2$ | industrial | 0–2 km | land/ocean | |
| 4 | 0.12 | 2.43 | 0.20 | 0.87 | $1.70\text{e}-4$ | 1.50 | $-1.0\text{e}-2$ | biomass | 0–2 km | land/ocean | |
| 5 | 0.12 | 2.67 | 0.17 | 0.70 | $2.05\text{e}-4$ | 1.50 | $-2.0\text{e}-2$ | biomass | 0–2 km | land/ocean | |
| 6 | 0.10 | 1.60 | 0.32 | 0.42 | $4.35\text{e}-3$ | 1.53 | $-3.2\text{e}-3/-9.0\text{e}-4$ | dust | 0–2 km | ocean | weak abs. |
| 7 | 0.10 | 1.60 | 0.32 | 0.42 | $4.35\text{e}-3$ | 1.53 | $-4.6\text{e}-3/-1.2\text{e}-3$ | dust | 0–2 km | land/ocean | strong abs. |
| 8 | 0.10 | 1.60 | 0.32 | 0.42 | $4.35\text{e}-3$ | 1.53 | $-1.3\text{e}-2/-3.5\text{e}-3$ | dust | 0–2 km | ocean | weak abs. |
| 9 | 0.10 | 1.60 | 0.32 | 0.42 | $4.35\text{e}-3$ | 1.53 | $-4.6\text{e}-3/-1.2\text{e}-3$ | dust | 4–6 km | ocean | moderate abs. |

The LUTs, as originally defined in Hasekamp et al. [50], contained up to 29 aerosol models, with a larger choice of industrial, biomass, and dust mixtures, also considering 2 altitudes (1–2 and 4–6 km) for all models. The current version of the PMAp algorithm presented here uses 9 of these models as listed in Table 3, which already represents a good starting list for demonstration of the PMAp ability to differentiate aerosol type. A later version of PMAp could extend this list of considered models.

LUT, containing TOA reflectance and the associated Stokes fraction for the 10 PMD bands identified in Table 1, are available for every aerosol model and for the following parameters:

- The aerosol optical thickness (from 0.1 to 4.0);
- The observation geometry: viewing zenith angle (VZA with 5° step from 0 to 60°), solar zenith angle (SZA with 5° step from 25 to 75°), and cosine of relative azimuth angle ($\cos(\text{RAZI})$ with step 0.1);
- The surface pressure (1013.0 hPa for ocean and 700.0, 1013.0 hPa for land);
- The surface contribution for land: surface albedo (from 0 to 0.8);
- The surface contribution for ocean: surface chlorophyll concentration (from $1.0\text{e}-5$ to $10.0\text{ mg}\cdot\text{m}^{-3}$) and surface wind speed (from 3.0 to $11.0\text{ m}\cdot\text{s}^{-1}$);

3.2.2. UV LUT

This LUT, used for the calculation of the Aerosol Absorbing Index, contains modeled reflectances for a Rayleigh-only atmosphere, i.e., without clouds and aerosols but including the surface. The LUT is provided dependent on solar zenith angle, satellite viewing angle, and relative azimuth angle for PMD-3 to PMD-6. In the PMAp retrieval, the LUT of PMD-4 around 340 nm and PMD-6 around 380 nm is used with the following parameters:

- The elevation (0–8 km);

- The observation geometry: viewing zenith angle (from 0 to 60°), solar zenith angle (SZA from 20 to 85°), and relative azimuth angle (step 20°, from 0 to 180°);
- The surface albedo (from 0.01 to 0.8);

3.2.3. Cloud LUT

This LUT is used for the conversion of the TOA reflectance into a cloud optical depth (COD) and contains the following parameters:

- The cloud optical depth (from 0 to 100);
- The observation geometry: viewing zenith angle (from 0 to 60°), solar zenith angle (SZA from 20 to 85°), and relative azimuth angle (step 20°, from 0 to 180°);
- The cloud albedo (from 0.01 to 0.8);

3.3. Step 1: Cloud/Aerosol Discrimination from Multi-Sensor Pre-Classification

3.3.1. Desert Dust Detection

In order to better identify desert dust aerosol over the ocean and land surfaces, including over bright surfaces, a dust detection scheme is applied in the early stages of the PMAp algorithm, based on the unified approach to aerosol remote sensing in the infrared spectral range developed by Clarisse et al. [25]. Following this approach, a desert dust index is calculated using the IASI measurements from one hundred channels selected in the infrared thermal spectra, and reference mean clear sky and polluted spectra (i.e., spectra affected by the presence of a selected aerosol type, which is represented in our case by desert dust). The index is determined by comparing the distance between polluted and clear sky spectra to the distance between measured and clear sky spectra. This dust index is a threshold to 3.0, a value estimated after looking at a large number of assumed clear and polluted observations (as described in [25]).

3.3.2. Volcanic Ash/Thick Dust Detection

A refined detection of volcanic ash and thick dust is possible thanks to the very rich spectral information. The following tests are applied to detect such events:

- A threshold (-2.2 °K) on the brightness temperature difference (BTD) between 10.8 μm and 12 μm AVHRR bands is widely used because dust and ash events cause a negative BTD due to the dust absorption at 10.8 μm (with a different threshold value for ocean and land) [51]. The separation between aerosol and clouds works best for ice clouds due to ice absorption at 12 μm . However, the test also delivers a lot of misclassifications due to low-level water clouds. Therefore, an additional test on the spatial homogeneity of AVHRR brightness temperature at 10.8 μm is also applied in a 3×3 pixel vicinity (ash/dust when the variance is lower than typically 0.1);
- A threshold on the GOME-2 UV Absorbing Aerosol Index (AAI) was calculated for the whole PMD footprint. This AAI was derived according to de Graff et al. [52]. The PMD-6 band around 380 nm was used to derive an effective surface albedo using the UV LUT (see Section 3.2.2), assuming a purely molecular atmosphere. Then, the PMD-4 band at 340 nm was used to derive the aerosol absorbing index using the effective surface albedo as input according to de Graff et al. [52]. Note this threshold was still under test and was not activated for the generation of the results presented in this paper;
- A test on IASI measurements in the thermal infrared spectral range combining two threshold tests on BTD at 10 μm and 12 μm (lower than -1 °K), and at 7.1 μm and 7.2 μm (higher than 2 °K). The second BTD was calculated between a background channel and the SO₂ ν_3 absorption band channel, which was by far the strongest absorption band of SO₂ in the mid-infrared (as described in [53]). This test was a simultaneous detection of coarse particles and SO₂, thus likely suggesting the presence of volcanic ash aerosol;

- Additional tests were applied for ocean only, using thresholds on the reflectance ratios $R(1.6 \mu\text{m})/R(0.87 \mu\text{m})$, $R(1.6 \mu\text{m})/R(0.63 \mu\text{m})$, and $R(0.87 \mu\text{m})/R(0.63 \mu\text{m})$. Pixels were considered as ash/dust when all ratios were higher than 0.70. Dust aerosols usually show a significantly weaker wavelength dependency than clouds or fine mode aerosols [54] in the wavelength range under consideration;

3.3.3. Initial Cloud Mask (First Guess)

The AVHRR operational cloud mask provided with the AVHRR level-1b product (cloud analysis information provided as part of the scene type identification) is used as a first-guess for PMAp [55]. For each GOME-2 pixel, an initial geometric cloud fraction CF_{geom} was defined using the number of cloudy AVHRR pixels n_{cloudy}^{1g} within the GOME-2 pixel (having $n_{colocated}$ AVHRR pixels) according to the first guess cloud mask.

$$CF_{geom}(GOME) = \frac{n_{cloudy}^{1g}(AVHRR)}{n_{colocated}(AVHRR)}$$

An AVHRR pixel is classified as not cloudy if four cloud detection tests, defined in [56], are in agreement:

1. Test *Ref*: reflectance in visible bands should not show high values (bright clouds);
2. Test *T4*: brightness temperature at $10.8 \mu\text{m}$ should not have low values, which are a sign of medium and high-level clouds;
3. Test *T4T5*: difference between brightness temperature at $10.8 \mu\text{m}$ and $12 \mu\text{m}$ should not give high positive values, which are a sign of thin cirrus presence;
4. Test *SpHo*: spatial homogeneity of the brightness temperature at $10.8 \mu\text{m}$ within a 3×3 AVHRR pixels box should not reveal high values, sign of a cloud edge, a thin cirrus, or a small cumulus (over water surfaces only).

In order to deal with the frequent situation of dust or ash aerosol transported above clouds, this cloud mask assessment is also performed when dust and ash have been detected previously and when the cloud fraction is $>90\%$. In this case, the retrieval scene is labeled as an aerosol-contaminated cloud.

3.3.4. Clear-Sky AVHRR Reflectances for Typical Clear Conditions

The retrieval of AOD was conducted for a GOME-2 PMD footprint. Each footprint contains various colocated AVHRR pixels because the spatial resolution of AVHRR is much finer than the spatial resolution of GOME-2. The initial cloud mask provided in the AVHRR L1B product was not sufficiently reliable, in particular for the discrimination of clouds from thick dust or aerosol events. As a consequence, improved estimation of the clear-sky conditions for all AVHRR pixels and bands is needed, in order to derive more reliable information about the cloudiness of GOME-2 pixels and for cloud decontamination of partially cloudy GOME-2 pixels.

The strategy in PMAp is to determine the clear-sky reflectance on the GOME-2 footprint for five different types of clear-sky conditions reported in Table 4. For every GOME-2 footprint, the clear sky AVHRR reflectances are estimated through pre-classification and removal of cloudy AVHRR pixels using the tests defined in Table 4. The selection of the most appropriate clear sky reflectance will be later described in Section 3.3.5.3 and Table 5.

Table 4. Different types of clear-sky conditions and the associated radiometric tests applied accordingly. The unfiltered clear-sky condition corresponds to the case for which the removal of cloudy pixels is applied without any specific filtering, i.e., applying all tests and types of removal.

| Name | Clear-Sky Condition | Test | | | | | | | | |
|------------|-------------------------------|------|------|----|-------|-----|---------|-----|----|----|
| | | Ref | SpHo | T4 | T4 T5 | BTD | VIS/NIR | Out | R4 | R3 |
| CS1-DUST | Volcanic Ash and extreme Dust | | | | | X | | | | |
| CS2-COARSE | Coarse Mode and Dust | X | X | X | X | | X | X | | |
| CS3-STD | Unclassified | X | X | X | X | | X | X | X | |
| CS4-FINE | Fine Mode | X | X | X | X | | X | X | X | X |
| CS5-IR | Thick Aerosol | | X | X | X | | | | | |
| Reference | Unfiltered Clear-sky | X | X | X | X | X | X | X | X | X |

Table 5. Aerosol classifications used within PMAp, the associated clear-sky conditions, and the default aerosol model considered for the AOD retrieval.

| Nr | Class | Surface | Characterization | Aerosol Models (Table 3) | Clear-Sky Condition (Table 4) | Default Model |
|----|-----------------------------------|------------|---|------------------------------|--|-----------------------|
| 0 | no dust/ fine mode | ocean | BTB dust tests negative and strong wavelength dependency of the reflectance between 0.6 μm and 1.6 μm . | 1–5 | CS5 | 1 |
| 1 | strong coarse mode | ocean | BTB dust tests negative and weak wavelength dependency of the measured signal between 0.6 μm and 1.6 μm | 6–8 | CS3 | 6 |
| 2 | biomass burning | not used | not used (placeholder) | | | |
| 3 | thick dust/volcanic ash | land/ocean | BTB dust tests positive, weak wavelength dependency in VIS/NIR (sea only), IASI SO ₂ test negative | 6–8 (ocean) 9 (land) | CS1 | 6 (ocean) 9 (land) |
| 4 | volcanic ash with SO ₂ | land/ocean | BTB dust tests positive, weak wavelength dependency in VIS/NIR (sea only), IASI SO ₂ test positive | 6–8 | CS1 | 8 |
| 15 | no classification | land/ocean | - | 1–8 (ocean) 2–5, 9 (land) | CS4 (ocean) Min[CS2, CS3, CS4 CS5] (land) | 1 (ocean) 2 (land) |

The following tests are considered for pre-classification and removal of cloudy AVHRR pixels within a GOME-2 footprint:

- Tests *Ref*, *SpHo*, *T4*, and *T4T5* are taken from the AVHRR cloud mask and defined in Section 3.3.3;
- Test *BTB*: lowest (highest negative) brightness temperature difference between 10.8 μm and 12 μm ;
- Test *VIS/NIR*: iterative removal of the coolest pixels at 10.8 μm as long as heterogeneity is observed in infrared (variance at 10.8 μm > 0.02), but homogeneity is observed in visible (variance at 670 nm < 0.05);
- Test *Out*: outlier correction through an iterative removal of (i) for the 3 reflective solar bands, the brightest pixel as long as the average of remaining pixels is lower than the median of AVHRR pixels over the GOME-2 footprint, and (ii) for the band 10.8 μm , the coolest pixel as long as the average of remaining pixels is higher than the median of AVHRR pixels over the GOME-2 footprint;
- Test *R4*: iterative removal of the coolest pixels until the variance of the radiance for 10.8 μm is below a threshold (0.002);

- Test R3: iterative removal of the brightest pixels until the variance of reflectance for 1.6 μm is below a threshold (0.002).

3.3.5. Pre-Classification of Aerosol (Aerosol Class)

In this section, a pre-classification of the aerosol model corresponding to the GOME-2 PMD footprint was performed as well as a selection of the associated aerosol models to be considered in the retrieval. If the class remains undefined through the following tests, then the default aerosol model is used, as described in Section 3.3.5.3.

3.3.5.1. Desert Dust and Ash

Desert dust and volcanic ash were detected in the earlier cloud/aerosol discrimination step of PMAp. In the case of an additionally positive IASI test, the aerosol class associated with these pixels was set to “thick dust/volcanic ash” or “volcanic ash with SO_2 ” if the IASI SO_2 test was positive (Table 5). Over the ocean, in case the cloud fraction from AVHRR was larger than 0.9, and the IASI dust test was positive, the pixel was classified as “ash contaminated cloud” (“aerosol contaminated cloud” if the IASI test is negative).

3.3.5.2. Fine/Coarse Mode Discrimination over Ocean

For observation over the ocean, the aerosol class can be distinguished between fine or coarse mode using a set of thresholds on the spectral ratios $R(1.6 \mu\text{m})/R(0.8 \mu\text{m})$ [fine mode when <0.7 , coarse mode when >0.8], and $R(0.8 \mu\text{m})/R(0.6 \mu\text{m})$ [this ratio is compared to the no-aerosol reference from the LUT; fine mode when ratio $<1.2 \times$ reference, and coarse mode when ratio $>1.4 \times$ reference]. Large aerosol particles (described as a combination of median radius and standard deviation of the lognormal distribution) show a weaker wavelength dependence compared to small particles in this wavelength range [54]. In these cases, the aerosol class is set to “strong coarse mode” representing dust or coarse-mode sea-salt. If a strong wavelength dependence is found, the aerosol model is set to “no dust/fine mode” (Table 5).

3.3.5.3. Selection of Clear-Sky Condition and Default Aerosol Model

Based on the tests performed in previous sections, Table 5 is used to select the associated clear-sky conditions of the GOME-2 PMD pixel ($R_{AVHRR-1}^{clearsky}$) to be used for the calculation of the final cloud fraction (see next section). The aerosol model to be used by default for the later retrieval of the AOD is also defined. When none of these tests have been able to identify a candidate class of aerosol or to derive a proper cloud fraction, the AOD will be retrieved assuming the default aerosol model, and the aerosol class is set to “No classification.”

3.3.6. Final Cloud Mask

A classification of the GOME-2 PMD footprint is finally proposed among:

- Case CS: clear-sky pixel;
- Case SCC: pixel with small cloud contribution for which AOD could be retrieved after cloud decontamination (i.e., reflectance will be corrected for cloud contamination);
- Case LCC: pixel with large cloud contribution and for which it will be impossible to retrieve an AOD;

The number of cloud-free AVHRR pixels n_{clear} into a PMD footprint is defined by the number of pixels identified as clear-sky in the previous section. Therefore, the final cloud fraction of the GOME2 PMD pixel, CF_{GOME} , can be derived by:

$$CF_{GOME} = 1 - \frac{n_{clear}(AVHRR)}{n_{colocated}(AVHRR)}$$

The GOME-2 pixel is labeled as clear-sky using radiometric criteria based on the difference between the average reflectance at 0.6 μm of AVHRR clear pixel, $\langle R_{AVHRR-1} \rangle_{n_{clear}}$,

and the average reflectance of all colocated AVHRR pixels, $\langle R_{AVHRR-1} \rangle_{n_{colocated}}$. The pixel is declared CS if one of the two following tests are fulfilled:

- The difference is smaller than a threshold: 0.006 for land, 0.0002 for the ocean;

$$| \langle R_{AVHRR-1} \rangle_{n_{clear}} - \langle R_{AVHRR-1} \rangle_{n_{colocated}} | \leq Threshold$$
- For ocean only, the relative difference between clear and colocated reflectance is smaller than a threshold (0.05);

For pixels not detected as clear-sky, a threshold is applied to the cloud fraction CF_{GOME} to decide if the cloud contribution is small (SCC) or large (LCC). This threshold was set to 65%.

3.3.7. Cloud Decontamination

For GOME-2 PMD pixels classified as small cloud contribution (SCC), it is possible to correct the pixel reflectance for the cloud contamination. This first-order correction uses the heterogeneity information from AVHRR channel 1. The decontamination is obvious for PMD12 because the GOME-2 and AVHRR wavelengths are similar (see Figure 3). The decontaminated PMD-12 reflectance, $R_{PMD12}^{cleared}$, is defined as the relative part of the PMD-12 reflectance only due to clear sky sub-pixels ($R_{AVHRR-1}^{clearsky}$ estimated in the previous section), and can be written as:

$$R_{PMD12}^{cleared} = R_{PMD12} \frac{R_{AVHRR-1}^{clearsky}}{\langle R_{AVHRR-1} \rangle_{n_{colocated}}}$$

Note that, for this GOME-2 PMD pixel, the associated cloud reflectance can be written accordingly as:

$$R_{cloud} = \frac{R_{PMD12} - (1 - CF_{GOME}) \cdot R_{PMD12}^{cleared}}{CF_{GOME}}$$

The correction of the other PMDi bands is more complicated because the wavelengths are rather different to AVHRR, but also because the footprints are shifted with respect to PMD-12 due to spatial aliasing. For other PMDi bands, the decontamination follows the same approach, but two aspects have to be adjusted. First, the average reflectance $\langle R_{AVHRR-1} (PMDi) \rangle_{n_{colocated}}$ and clear sky reflectance $R_{AVHRR-1}^{clearsky} (PMDi)$ derived from AVHRR channel 1 and initially calculated for PMD-12 have to be recalculated for the exact PMDi footprint that slightly differs from PMD-12 due to spatial aliasing. Second, it is necessary to recalculate an effective cloud fraction and cloud reflectance for the PMDi band of interest. The effective cloud fraction CF_{eff} is calculated for every PMDi band combining average and clear sky reflectances with the cloud reflectance R_{cloud} from band PMD-12 [38,57,58] as:

$$CF_{eff} = \frac{\langle R_{AVHRR-1} (PMDi) \rangle_{n_{colocated}} - R_{AVHRR-1}^{clearsky} (PMDi)}{R_{cloud} - R_{AVHRR-1}^{clearsky} (PMDi)}$$

The cloud reflectance R_{PMDi}^{cloud} for band PMDi is calculated based on an extrapolation of the cloud reflectance R_{cloud} initially estimated for band PMD-12 using a LUT considering a Lambertian cloud layer at 700 hPa with a cloud albedo of 0.8, Rayleigh scattering, and different surface reflectances [59]. Finally, the decontaminated reflectance $R_{PMDi}^{cleared}$ can be estimated for all PMDi bands according:

$$R_{PMDi}^{cleared} = \frac{R_{PMDi} - CF_{eff} \cdot R_{PMDi}^{cloud}}{1 - CF_{eff}}$$

This decontamination cannot be applied to polarized reflectance as no polarized information is available for GOME-2 at the sub-pixel level, and in that case, the retrieval will be only based on unpolarized reflectance.

3.4. Step 2: Retrieval of AOD for Every Candidate Aerosol Model

In the second step, the AOD is retrieved for all candidate aerosol models in the aerosol class of the pixel under consideration, using one single band depending on the surface type. Additionally, the surface contribution, parametrized as a function of chlorophyll pigment concentration, can be estimated for clear sky pixels over the ocean.

3.4.1. Interpolation of the LUT

The derivation of the AOD relies on a LUT approach to optimize the processing time. As described in Section 3.2.1, the LUTs contain TOA reflectance and Stokes fraction for PMD bands for a given number of parameters, among which are the viewing and solar geometries. This step interpolates the LUT to the exact geometry of the pixel under consideration, using interpolation in the scattering angle domain between the two nearest neighbor scattering angles.

3.4.2. Identification of Observations Significantly Perturbed by Sun Glint

For geometries contaminated by sun glint, an alternative retrieval of AOD is used (see next section). It is difficult to accurately predict the sun glint contribution-based only on the surface wind speed v_{wind} [ECMWF] taken from ECMWF forecasts, with a maximum forecast range of 6 h. The aim of this filtering is to identify observations for which the uncertainty due to sun glint would represent a significant part, typically 50%, of an aerosol reference signal assumed to be sea-salt aerosol (model 1 in Table 4) with an AOD of 0.3. For this, a twofold approach is used. The first is purely geometrical, checking if the viewing geometry is close to the exact specular geometry. If this angular difference is smaller than 15° , the view is considered to be too significantly affected by sun glint and is not retrieved. The second approach is radiometric. A reference aerosol signal is calculated for PMD-12 as the difference between the TOA reflectance with aerosol, $R_{refaerosol}$, and the TOA reflectance in the absence of aerosol, $R_{noaerosol}$. An indication of the degree to which the sun glint may impact the reflectance for the corresponding pixel configuration (i.e., solar and viewing geometries) can be assessed based on the difference between $R_{reference}$ calculated for 2 wind speeds. Therefore, a pixel is considered to be too significantly perturbed by sun glint, and as a consequence not retrieved, if:

$$R_{refaerosol}(v_{wind}[ECMWF]) - R_{noaerosol}(v_{wind}[ECMWF]) < 0.5 \times \left| R_{noaerosol}(v_{wind}^{max}) - R_{noaerosol}(v_{wind}^{min}) \right|$$

where v^{max} and v^{min} are the minimum and maximum wind speed values of the LUT. This consequently leads to additional gaps in the PMAp retrieval for the Eastern part of the swath and moderated latitudes. Another criterion is used to identify and exclude situations for which the reference aerosol signal $R_{refaerosol}$ is less than 20% of the aerosol free signal $R_{noaerosol}$ (which includes sun glint) according to:

$$\left[R_{refaerosol}(v_{wind}[ECMWF]) - R_{noaerosol}(v_{wind}[ECMWF]) \right] < 0.2 R_{noaerosol}(v_{wind}[ECMWF])$$

In that case, because the aerosol signal in the TOA reflectance is too limited, the alternative retrieval of AOD will be used (next section).

3.4.3. Retrieval over Ocean

For the retrieval of AOD, the surface contribution has to be considered. For cloud-free pixels (CS), chlorophyll pigment concentration Chl is estimated, jointly with a first guess

aerosol optical depth AOD_{1g} , through a χ^2 minimization using reflectance of three PMD bands R_{PMD} : PMD-7 (414 nm), PMD-10 (554 nm), and PMD-12 (640 nm).

$$\chi^2 = \sum_{PMD} \frac{(R_{PMD} - R_{LUT}(AOD_{1g}, Chl))^2}{R_{LUT}(AOD_{1g}, Chl)}$$

For partly cloudy pixels (SCC), a global default value of $1e^{-5}$ mg/m³ (low chlorophyll load) was assumed for Chl . Once the chlorophyll pigment concentration is known, the AOD is estimated for every candidate aerosol model by interpolation of R_{LUT} from LUTs using reflectance in PMD-12 (decontaminated reflectance for partly cloudy pixels).

For clear pixels with a significant sun glint contribution (identified in the previous section), an alternative retrieval relies, in addition, on Stokes fraction because both aerosol and sun glint show a significant polarized signature. The global default value was assumed for Chl . Then, the AOD was retrieved through a χ^2 minimization using reflectance from the PMD-9 band (522 nm).

$$\chi^2 = \frac{(R_{PMD9} - R_{LUT}(AOD))^2}{R_{LUT}(AOD)} + \frac{(q_{PMD9} - q_{LUT}(AOD))^2}{q_{LUT}(AOD)}$$

If the χ^2 difference between measured and modeled reflectance and Stokes fraction were both below a pre-defined threshold, the minimization was recalculated using only the Stokes fraction. If the difference is still not fulfilling the criterion, the retrieval fails.

3.4.4. Retrieval over Land

Over land, the AOD was calculated from PMD-8 (463 nm) because the surface albedo remains low for most areas in this band. For higher wavelengths, the contrast between aerosol and the surface becomes much less favorable [17]. It is also the rationale used for the MODIS deep blue AOD retrieval over land [33].

The PMAp retrieval over land was based on a priori information on the surface using the GOME-2 Lambertian-Equivalent reflectance database [59]. This GLER database provides a climatological value for the monthly surface reflectance. An angular dependence from the GOME-2 viewing angle was also provided in order to account for the bidirectional variation of the surface reflectance. As a consequence, the surface reflectance was derived from GLER after temporal interpolation for the date of observation and correction for the viewing angle. If the surface reflectance in PMD-8 was found to be significantly brighter than for PMD-7, the retrieval alternatively switches the calculation of AOD to PMD-7. In all cases, the surface pressure was taken into account again using the operational ECMWF 6 hourly forecast.

As for retrieval over the ocean, the AOD was estimated for every candidate aerosol model by interpolation on R_{LUT} from LUT using reflectance in PMD-8 (decontaminated reflectance for partly cloudy pixels).

3.5. Step 3: Selection of the Aerosol Model and its Associated AOD

The final AOD can be determined once the aerosol model AM is identified. For this, χ^2 minimizations on reflectances R and Stokes fractions q are performed using different sets of bands for unpolarised reflectance (for n_{PMD} bands) and a polarized q-Stokes fraction (for n_{PMDq} bands). The χ^2 function is written:

$$\chi^2 = \frac{1}{n_{PMD} + n_{PMDq}} \cdot \left(\sum_{n_{PMD}} \frac{(R - R_{LUT}(AOD, AM))^2}{R_{LUT}(AOD, AM)} + \sum_{n_{PMDq}} \frac{(q - q_{LUT}(AOD, AM))^2}{q_{LUT}(AOD, AM)} \right)$$

The Stokes Fractions are considered in the χ^2 function for clear-sky pixels only because no cloud decontamination is available for polarization. Cases for which the reflectance

from the LUT is lower than a threshold: $R_{LUT} < 0.002$, and $q_{LUT} < 0.05$ over ocean or 0.1 over land are also discarded from the χ^2 function.

Over land, the fit was performed in two steps. First, the fit was performed on the reflectances from PMD-7 to -12 (412–640 nm) only. Bands with a surface albedo above 0.05 were excluded, and finally, all models with $\chi^2 > 0.0005$ and $\Delta\chi^2/\chi^2 > 1$ were also excluded. The Stokes fractions from PMD-7 to -14 (414–799 nm) were fitted to the remaining models if the criteria above were fulfilled. Models were excluded using the same criteria. The default aerosol model from the corresponding aerosol class was selected if it was still included in the possible models, otherwise, the aerosol model with the lowest χ^2 was selected.

For clear sky pixels over the ocean, the fit takes into account the reflectance of PMD-7 to -14 (414–799 nm) and Stokes fractions of PMD-9 to -14 (522–799 nm). The model with the lowest χ^2 was selected if the fit was significantly better compared to the default model ($\Delta\chi^2 < 0.0005$ or $\Delta\chi^2/\chi^2 < 1$). If this criterion is not fulfilled or if the pixel is partly cloudy, the default aerosol model from the corresponding aerosol class is selected.

In both ocean and land cases, a selection of the aerosol model cannot be performed for partly cloudy pixels because Stokes fractions were not decontaminated as performed for reflectance. As a consequence, the default aerosol model from the corresponding aerosol class was selected.

Once the aerosol model is known (selected or default), the associated AOD can be considered as the final AOD retrieval. In the case of negative AOD values, the AOD is set to 0. These null values, considered as not fully physical, will be discarded for the evaluation of the performance.

3.6. Calculation of Uncertainty

The retrieved AOD is associated with an estimation of the uncertainty. It is very challenging to provide an uncertainty able to fully characterize a representative error for the given pixel. Here, a statistical approach is used to provide a randomized error suitable for assimilation purposes. The uncertainty is defined as the standard deviation of a set of AOD (at least 30 values) recalculated based on the same retrieval but with changes on inputs or assumptions. The AOD uncertainty is recalculated for the following cases:

- Angular interpolation: nearest neighbours for SZA, VZA, and RAZI are used instead of the values interpolated to the actual measurements;
- Aerosol model: all aerosol models from Table 4 are used for the fit on the retrieval instead of those limited to the aerosol class;
- Cloud decontamination: maximum and minimum values are obtained from the scatter between averaged AVHRR reflectance and the GOME-2 reflectance (standard deviation of the linear fit in Figure 2).
- Surface contribution: ranges of wind speed and chlorophyll pigment concentration are used for ocean, and alternative surface albedo (the GOME-2 albedo from Tilstra et al. [59] and the black-sky albedo from MERIS [60]) are used for land;

3.7. Cloud Optical Depth

A Cloud Optical Depth parameter (COD) is provided in PMAp as a side parameter in addition to the aerosol characterization. This cloud parameter is provided for information and is designed for monitoring and validation, as well as to support the interpretation of the aerosol product. The COD is not designed as a real cloud parameter because it is derived assuming fixed microphysical properties within the cloud model.

The retrieval of COD relies on a LUT calculated for a typical cloud model and assuming a given surface albedo. The surface albedo is either derived from the clear-sky reflectance if the pixel is partly cloudy (use of aerosol LUT to invert the albedo knowing the aerosol) or from the GOME-2 LER surface albedo climatology [59] if the pixel is fully cloudy. Once the surface albedo is known, the LUT is interpolated to the exact geometry of the pixel, and the COD is calculated for PMD-12. The COD is finally provided at 550 nm to be consistent with AOD.

4. Results and Validation

4.1. Qualitative Evaluation

The thorough validation and assessment of the performance of a retrieved aerosol product is a complex and large task. In this section, the goal is not to provide full validation of the PMAp products, which will be more extensively addressed in an upcoming dedicated paper, but to demonstrate the good potential of the retrieval, qualitatively, but also quantitatively. The following results are based on the last version of the operational near-real-time PMAp product (version 2.2.4) [28].

Figure 4-top illustrates a typical daily retrieval of the AOD for Metop-B for 21 September 2020. The global distribution of AOD is obtained for the part of the swath not affected by sun glint, which creates an artificial reduction of the swath over the ocean. Aerosol patterns can be identified over many different locations, oceans, or continents. Figure 4-bottom shows the same daily retrieval as Figure 4-top but combines the results from the three Metop platforms. The global coverage was obviously much better, and the qualitative consistency between the three products was clear. The major aerosol events were captured worldwide: biomass burning from California in Northern America, from Amazonia, South America, and Siberia, the usual desert dust plume crossing the Atlantic from Africa to America, multiple desert dust events over North Africa, Arabia, and Asia, and probably anthropogenic pollution in Asia. A generally good spatial consistency was observed, including for the land to sea transition (e.g., in Africa, Arabia, and Northern America).

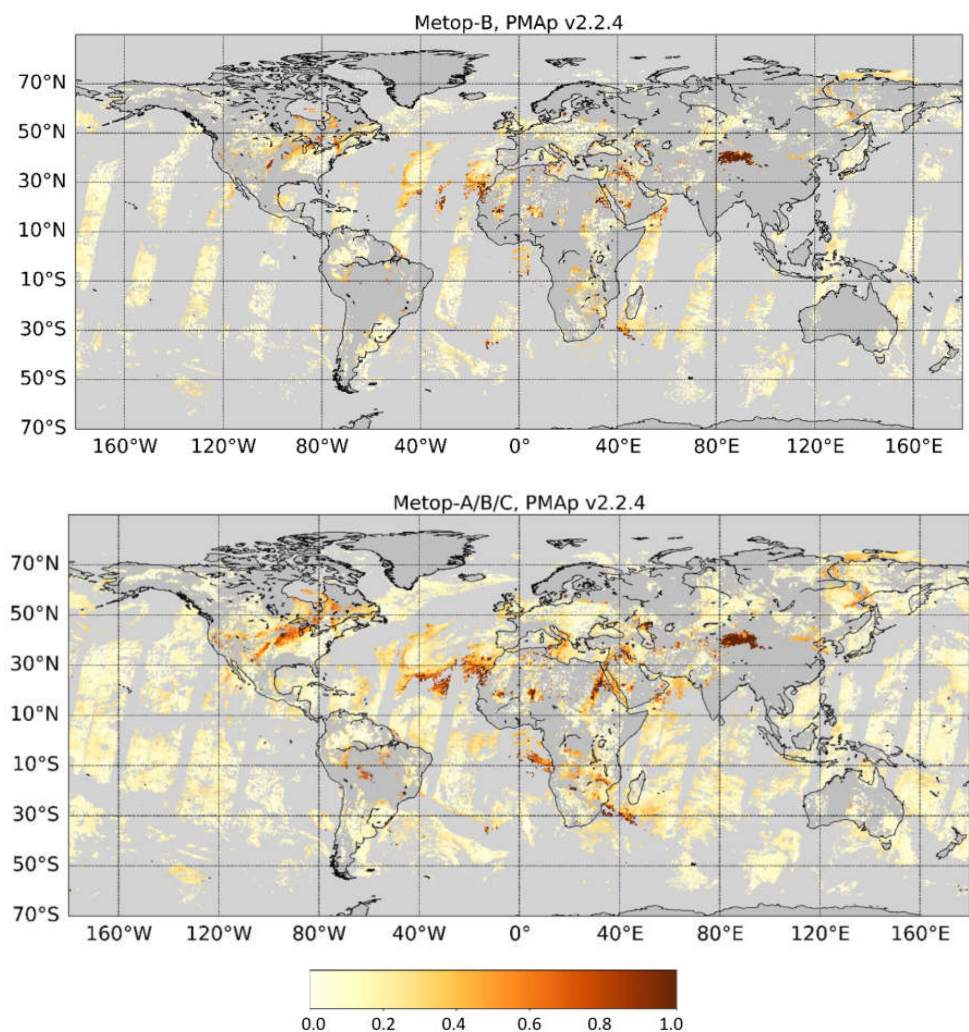


Figure 4. Global daily aerosol optical depth retrieved by PMAp for the 21 September 2020. AOD only based on Metop-B (top) and based on the combination of the three Metops (bottom).

Figure 5 shows the associated output parameters provided in the PMAp aerosol product. In Figure 5 top-left, the retrieval approach was presented, i.e., which branch of the algorithm was used in terms of cloudiness and surface type. The situation over the ocean was dominated by cloud-free and partly cloudy cases. Over land, the retrieval approach was much more variable. As there is much more contrast in the surface contribution over land, cloud-free and partly cloudy conditions were combined with dark, nominal, or bright surfaces. It is interesting to note that, despite the spatial heterogeneity of the retrieval approach over land, the AOD in Figure 4 appears spatially consistent. Figure 5 top-right illustrates the aerosol class selected by PMAp. The class remains mostly undetermined over land, where the main distinction is made for dust aerosol. Over the ocean, the aerosol class is mostly dominated by fine mode, with some regular coarse class observed, for instance, in California, the Indian ocean, or Eastern Australia. The desert dust identification appears nicely consistent between ocean and land. In this example, no ash was detected (but it was clearly observed on other days for recent volcanic eruptions such as Etna, La Soufrière, Raikoke, as previously demonstrated also in Clarisse et al. [25,61]). Finally, partly cloudy situations were very frequent cases. This is mostly a consequence of the GOME2 footprint size, which is very large (200 km² for Metop-A and 400 km² for Metop-B and -C). In Figure 5 bottom-left, the uncertainty associated with the AOD value is illustrated. It was observed that, over the ocean, the uncertainty was usually small. For land, the uncertainty was clearly proportional to the AOD itself, as correlation with Figure 4 can be seen. Very high uncertainties were observed for bright surface conditions for which it is known that the AOD retrieval is more problematic. Figure 5 bottom-right illustrates the cloud fraction as seen by AVHRR. It is interesting to note that the AOD retrieval provided in Figure 4 for partly cloudy conditions was, in general, spatially consistent with the AOD retrieval for cloud-free conditions (mostly visible over the ocean, especially for Southern latitudes). It was a qualitative confirmation that the cloud decontamination of the GOME2 pixel performed in PMAp was valid.

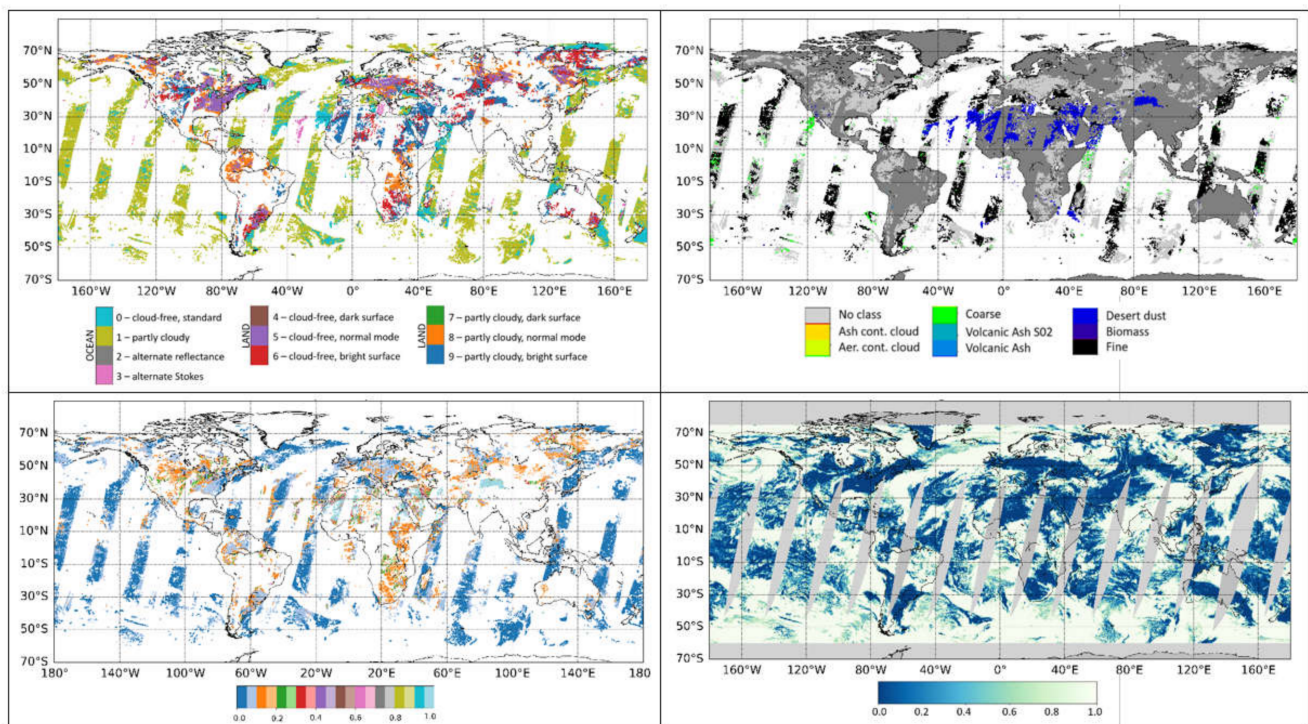


Figure 5. Parameters associated with the AOD in the PMAp aerosol product. Retrieval approach (top-left), aerosol class (top-right), AOD uncertainty (bottom-left), and cloud fraction (bottom-right) associated with the AOD illustrated in Figure 3.

Figure 6 shows the AOD retrieved by MODIS-Terra using the Merged Deep Blue/Dark Target algorithm (version 6.1.), and the VIIRS Deep Blue product, which is a combination of the Deep Blue retrieval over land and the Satellite Ocean Aerosol Retrieval (SOAR) algorithm over the ocean (this product called Deep Blue, includes data over-water retrievals as well) [62]. These aerosol products are regularly used as a reference because of their maturity level and because their performance was extensively documented [18–20,63]. As can be seen, Figure 4-bottom shows patterns very similar to those observed in Figure 6 by both MODIS and VIIRS. This is true for all events in Africa, America, Siberia, Asia, as well as over the oceans. This demonstrates how PMAp is able to retrieve very relevant aerosol information, spatial features, as well as the order of magnitude of the AOD. Excessive cloud screening can possibly be observed in PMAp over bright surfaces (this is very obvious when compared to VIIRS, which has a larger swath and is much more reasonable when compared to MODIS). This is partly a consequence of the large GOME-2 footprint for which AOD cannot be retrieved when significant cloud contamination exists.

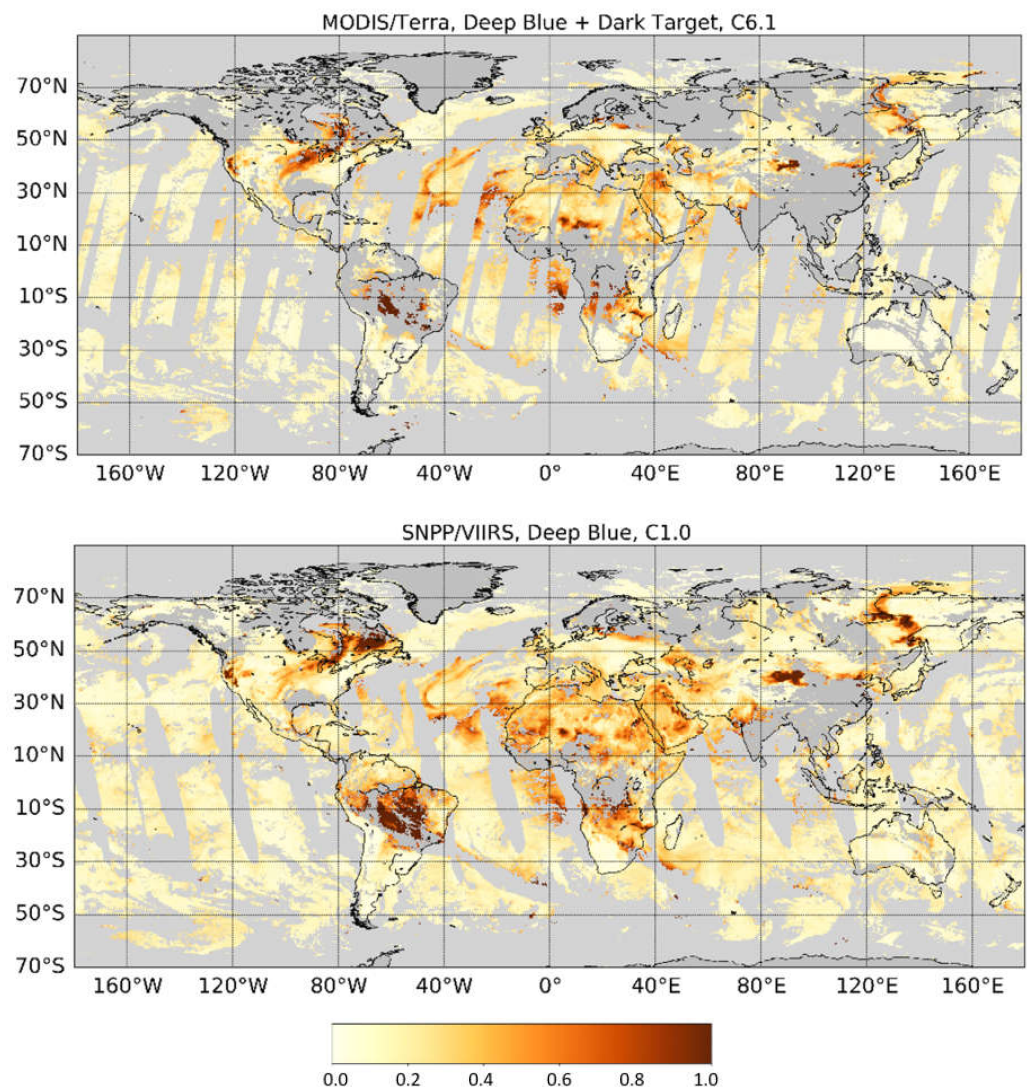


Figure 6. AOD derived from MODIS-Terra (top) and VIIRS (bottom) for 21 September 2020. The MODIS AOD is based on the collection 6.1 merged Deep Blue/Dark Target retrieval. The VIIRS AOD is based on the Deep Blue/SOAR retrieval.

Figure 7 illustrates the average AOD for the period of 12 days in September 2020. This specific period was chosen because of an interesting peak in aerosol events that occurred in summer 2020. It can be seen that PMAp captures most of the aerosol events

occurring around the world. A giant biomass-burning plume, coming from California, crossing North America, moving through the North Atlantic, and finally reaching the North-Western European coasts. Other biomass burning events occurred in South America, from Amazonia with a plume crossing South Atlantic, in South Africa, or Eastern Siberia [64]. Dust events were observed in Arabia and North Africa, crossing the Atlantic toward the west. Extreme pollution in Xinjiang Chinese province (dust event, coal fires, and industries in the Tarim Basin and Ala Shan plateau [65]) was also well captured, and with a smaller magnitude around the Beijing basin, in North India, or Indonesia [66].

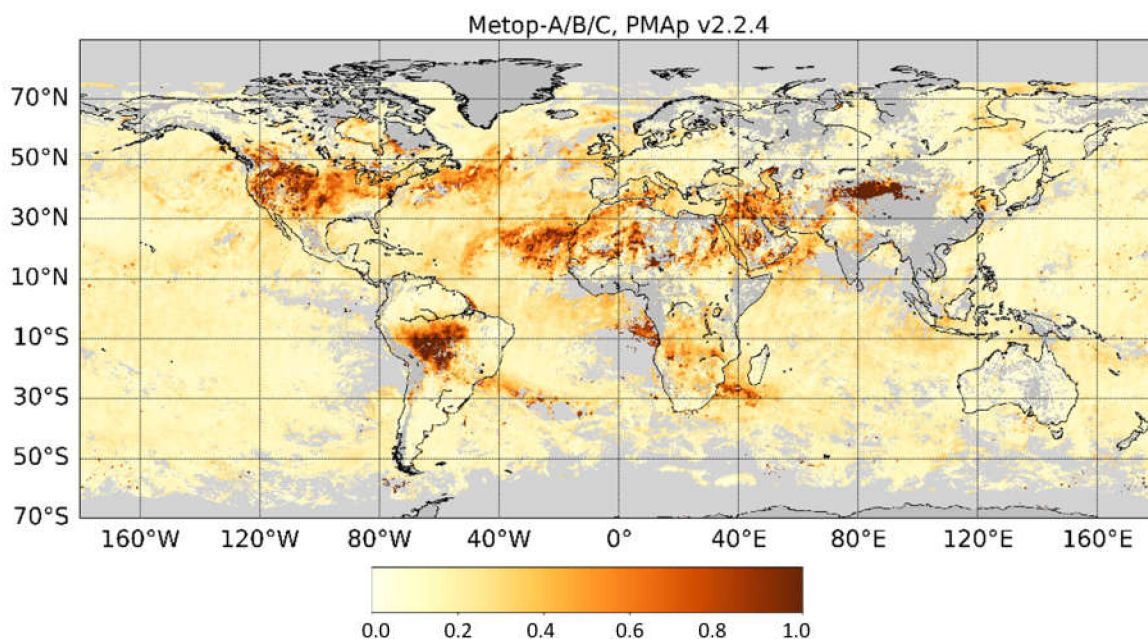


Figure 7. Average AOD derived from PMAp for Metop-A, B, and C on 10–21 September 2020.

4.2. Quantitative Evaluation Using Ground-Based Measurements

The qualitative evaluation described in the previous section already provides good information on the PMAp behavior and its level of performance, but a more quantitative evaluation of the performance can be derived through matchups with ground-based measurements. Here we used the AERONET ground-based network of sun-photometer data from a widespread network of about 130 sites, which allows a statistically significant comparison of the PMAp output against well documented and quality-controlled ground-based data [67]. AERONET Level 2.1 data were retrieved at 550 nm under cloud-free conditions using a direct sun inversion algorithm and were characterized by pre- and post-field calibration, cloud screening, and general quality assurance.

The PMAp retrieval performance was evaluated for two time periods, June–September 2013 (validation period 1) and February–May 2015 (validation period 2). These periods were historically adopted as reference periods for the evaluation of regular upgrades of the retrieval because the processing capabilities remained limited. They were defined in order to provide a large number of observations for exact spatiotemporal collocation with ground-based observations, but moreover, to allow the analysis to be carried out under representative atmospheric conditions for different seasons. Only Metop-A and –B can be evaluated for these periods because Metop-C was launched later in 2018. Note also that a reprocessing of the complete 2006–2019 Metop time series is ongoing in the context of climate data record generation, and this will allow the confirmation of the performance described in this analysis over the entire Metop archive. The analysis was separated for land and ocean surface measurements, and the validation procedure has been carried out as follows:

1. Collect AERONET measurements (level 2.1) within a 30-min time window around a Metop overpass and for stations below 2000 m in altitude;
2. Land: identify all corresponding GOME-2 measurements in a 30 km circle around the station;
3. Ocean: identify all corresponding GOME-2 measurements in a 30 km circle around the station (located on an island or at the coast);
4. Calculate the average PMAp AOD and plot the minimum and maximum value around the station;
5. If a quality assured AERONET measurement at 550 nm wavelength is not available, the AERONET value is interpolated at 550 nm from the neighboring spectral measurements;
6. Calculate the regression parameters for the whole matchups.

Figures 8 and 9 present the scatter plots of PMAp AOD at 550 nm as a function of the AOD derived from AERONET in situ measurement, for land and ocean surfaces, and for Metop-A and -B. Statistics were calculated in terms of slope, offset (representing the slope and offset of the best fit line), Pearson correlation coefficient (R), root mean square error ($RMSE$), and the number of points (N) of the linear regression, and all values were reported in Table 6. Figure 10 provides a visualization of values provided in Table 6 for every case: slope, offset, R , and $RMSE$, ocean or land, 2013 or 2015 validation periods.

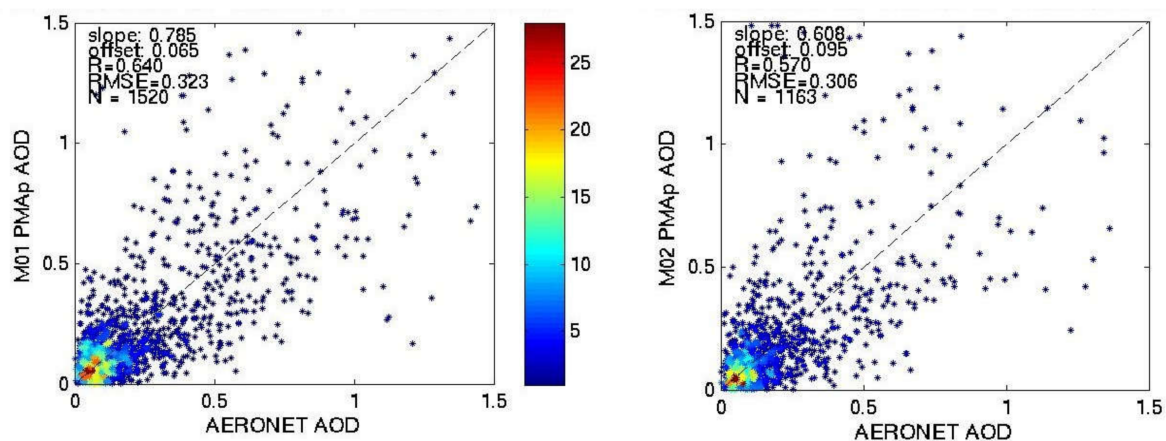


Figure 8. Scatter plot of the measurements for the validation period in 2015 for land sites: AOD at 550 nm from PMAp/Metop-B (left panel) and -A (right panel) is plotted versus the corresponding AERONET AOD measurements. The color illustrates the density of the measurements.

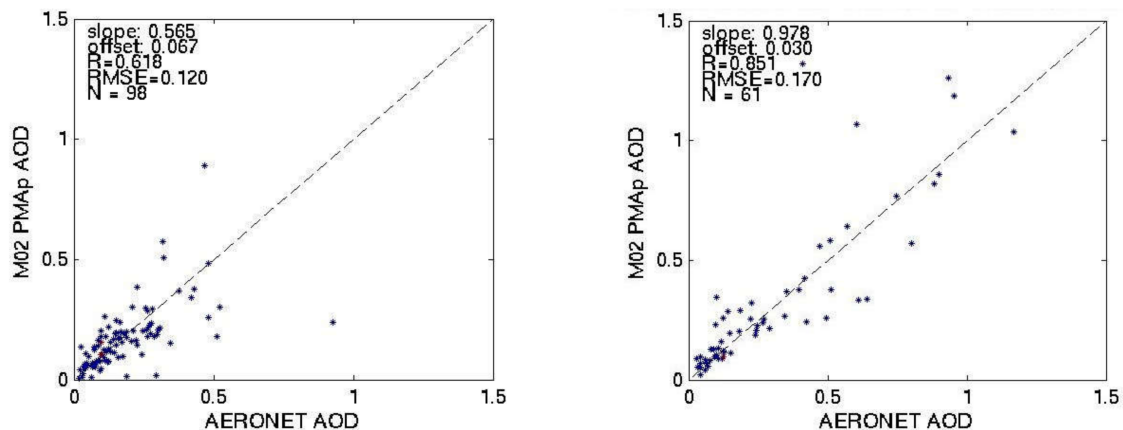


Figure 9. Scatter plot of the comparison of PMAp-A measurements with AERONET over the ocean, and for the validation period 1 in 2013 (left), and 2 in 2015 (right).

Table 6. PMAp AOD against AERONET AOD: summary of the performance for both Metop –A (in grey) and –B, for the two reference periods in June–September 2013 and February–May 2015, and over land or ocean. Filtered data refers to cloud-free retrieval cases, excluding bright surface conditions. Statistics provided are the number of matchups (*N*), the slope, offset, correlation coefficient (*R*), and root mean square error (*RMSE*) of the linear regressions.

| Metop | Period | Surface | Data | <i>N</i> | Slope | Offset | <i>R</i> | <i>RMSE</i> |
|-------|--------------|---------|----------|----------|-------|--------|----------|-------------|
| A | Jun–Sep 2013 | ocean | all | 98 | 0.56 | 0.06 | 0.61 | 0.12 |
| B | Jun–Sep 2013 | ocean | all | 119 | 0.43 | 0.10 | 0.49 | 0.25 |
| A | Feb–May 2015 | ocean | all | 61 | 0.97 | 0.03 | 0.85 | 0.17 |
| B | Feb–May 2015 | ocean | all | 81 | 0.99 | −0.02 | 0.75 | 0.22 |
| A | Jun–Sep 2013 | land | all | 853 | 0.92 | 0.04 | 0.58 | 0.30 |
| A | Jun–Sep 2013 | land | filtered | 150 | 1.05 | −0.04 | 0.70 | 0.13 |
| B | Jun–Sep 2013 | land | all | 986 | 1.15 | 0.00 | 0.56 | 0.32 |
| B | Jun–Sep 2013 | land | filtered | 127 | 0.83 | 0.00 | 0.80 | 0.13 |
| A | Feb–May 2015 | land | all | 1160 | 0.60 | 0.09 | 0.57 | 0.30 |
| A | Feb–May 2015 | land | filtered | 356 | 0.50 | 0.07 | 0.74 | 0.31 |
| B | Feb–May 2015 | land | all | 1520 | 0.78 | 0.06 | 0.64 | 0.32 |
| B | Feb–May 2015 | land | filtered | 298 | 0.61 | 0.04 | 0.76 | 0.24 |

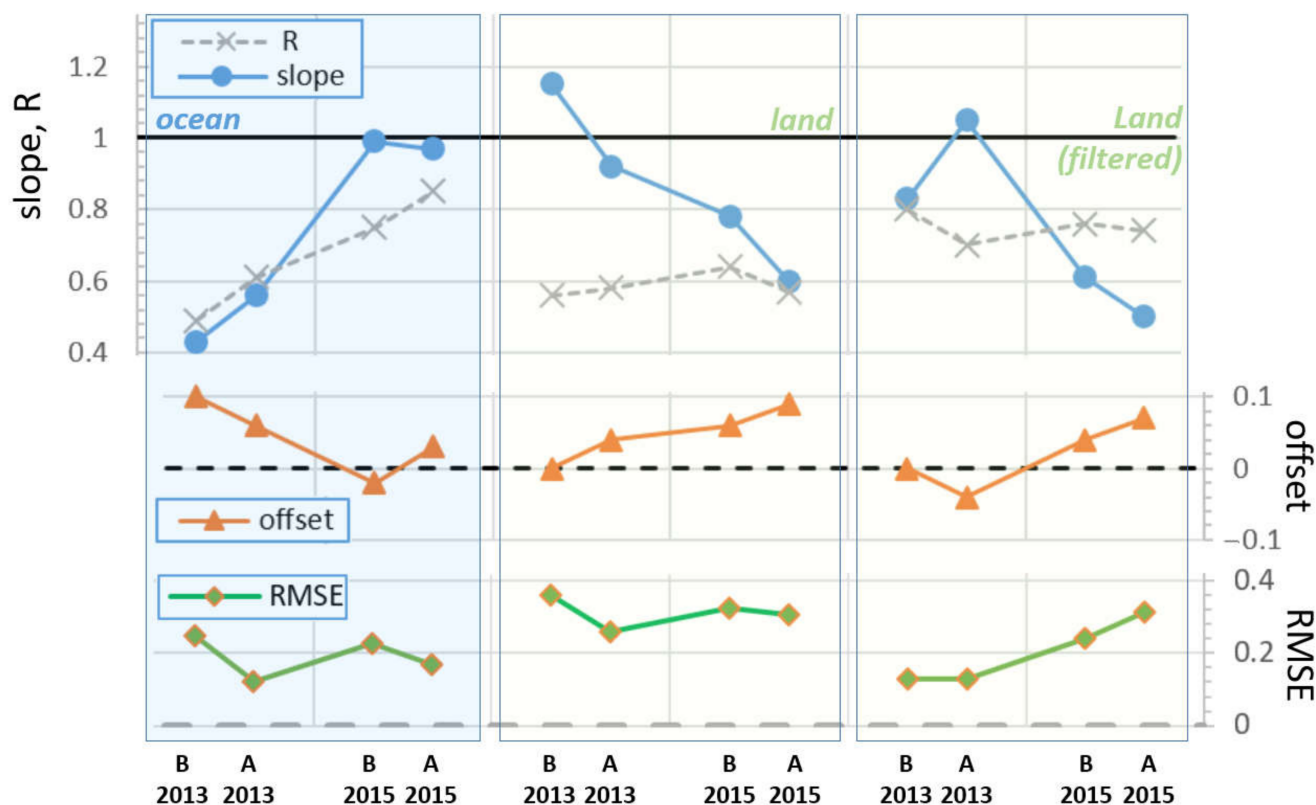


Figure 10. Performance of PMAp based on the matchups with AERONET measurements for Metop-A, -B, for the two reference periods in 2013 and 2015, and over the ocean (left) and land (middle) and land in the case of filtered data (right). Values for slope, *R*, offset, and *RMSE* is taken from Table 6. The black plain and dashed lines represent the perfect performance with slope/*R* equal to 1 (plain) and offset/*RMSE* equal to 0 (dashed).

In Figure 8, the distribution over land is quite similar for Metop-A and -B for the validation period in 2015 (the 2013 validation period is not presented because it shows approximately the same distribution, and the statistics are provided in Table 6). As also shown in Figure 10, the correlation was close to 0.60, the slope between 0.70 and 1.1, and the offset between 0.00 and 0.09. An additional statistic was provided over land by filtering

the data and discarding measurements associated with partly cloudy retrievals (about 50% of all retrieval cases) or bright surfaces (50% of cloud-free cases), situations for which a lower performance can be expected. These “filtered data” represent approximately 20% of the total number of matchups over land. As anticipated, it can be observed from Table 6 and Figure 10 that filtered data generally provide much higher performance in terms of correlation with values around 0.80 and also with a slight reduction of offset. On the other hand, the performance of all data (instead of filtered) shows a comparable slope and offset. The *RMSE* was found to be twice as large over land than the ocean, but once restricted to filtered data, the *RMSE* becomes roughly comparable over ocean and land. This demonstrates the reasonably good ability of PMAp to decontaminate for partly cloudy pixels, as described in Section 3.3.7.

In Figure 9, Table 6, and Figure 10, a significant difference is observed over the ocean between 2015 and 2013 for all parameters (offset, slope, and *R*). As Metop-A remains very consistent with Metop-B, this could be interpreted as a difference in terms of geophysical conditions between 2013 and 2015 (as also seen in the MODIS time series [68]), with PMAp having more difficulty in the retrieval of heavy dust events, which were more frequent in the 2013 validation period. Nevertheless, the comparison in Figure 9 of the 2013 and 2015 validation campaign does not qualitatively show very different scatter plots. The number of matchups is reduced due to the limited number of AERONET stations suitable for the oceanic environment. Therefore, the numbers provided for the overall performance remain very sensitive to outliers.

Figure 11 illustrates a comparative time-series of AOD derived from PMAp (with Metop-B) and AERONET for three representative sites for the validation period in 2013. The ability of PMAp to retrieve the temporal dynamics and change of the aerosol load, in the sense of day-to-day variation as observed by AERONET, is clearly demonstrated. For some days, the agreement with AERONET is quasi-perfect. However, for other days the difference in AOD can reach 0.05 or up to 0.1. When extreme dust events occur, such as over Valladolid in end-June 2013, the error in AOD can be larger (up to 0.45 in that case), but these situations are globally exceptional. The same type of time series is observed from PMAp AOD derived from Metop-A (not shown here). In addition, the same conclusion can be derived from Figure 12 for the validation period in 2015.

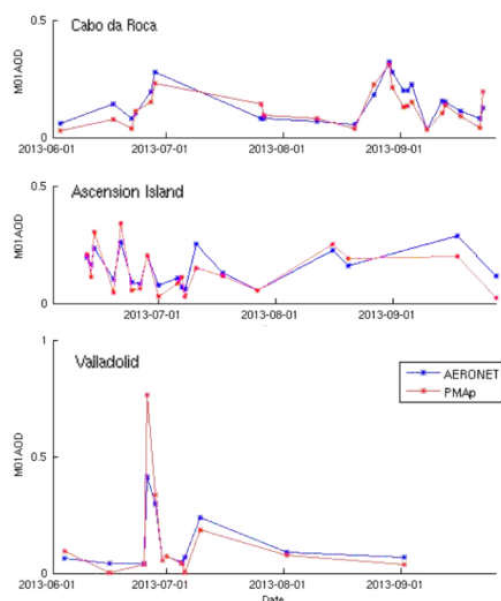


Figure 11. Time series of the PMAp AOD at 550 nm for validation period 1 compared to the AOD retrieved from Metop-B and for 3 AERONET sites: Cabo da Roca, Ascension Island, and Valladolid.

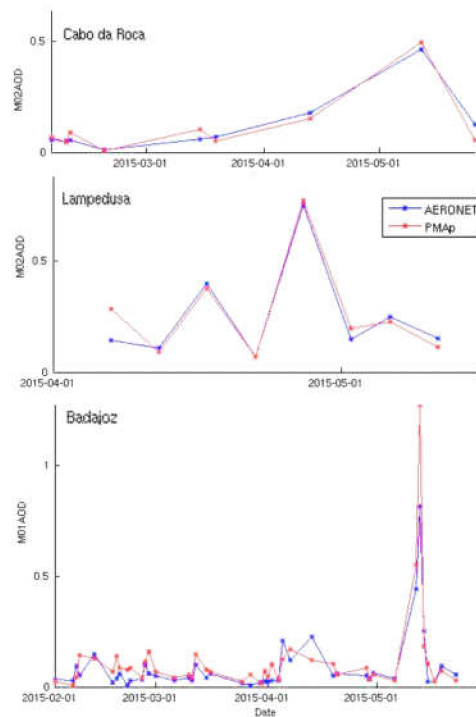


Figure 12. Time series of the AOD at 550 nm for validation period 2 compared to the AOD retrieved from Metop-B and for 3 AERONET sites: Cabo da Roca, Lampedusa, and Badajoz.

5. Conclusions and Perspectives

This paper describes the Polar Multi-Sensor Aerosol Product (PMAp) operational aerosol retrieval. The PMAp algorithm is based on a multi-sensor single-platform approach, synergistically exploiting observations from GOME-2, AVHRR, and IASI onboard the Metop satellites. Aerosol optical properties, as Aerosol Optical Depth at 550 nm wavelength and a PMAp tailored set of aerosol classes, are globally retrieved over the ocean and land surface at a spatial resolution of $10 \text{ km} \times 40 \text{ km}$ ($5 \text{ km} \times 40 \text{ km}$ for Metop-A) and are available within 1.5 (maximum 3) hours from sensing.

The PMAp algorithm is separated into three main steps. Step 1 consists of a preliminary aerosol optical properties classification, as well as cloud masking and cloud corrections, making use of the different spectral and spatial sampling features of the different sensors. In step 2, the radiative transfer calculations are carried out using specific GOME-2 PMD channels, retrieving a set of candidate AOD values for all the aerosol optical property models provided by the LUT. Finally, in step 3, the best fit using a least-squares minimization of the pre-selected aerosol properties and related AODs to all GOME-2 PMD channels provides the final AOD and aerosol class. Calculation of the error in AOD is also performed based on a standard deviation of a set of AOD values computed using variations in the input data.

Examples have been presented of daily and monthly averaged maps as derived both from Metop-A and Metop-B, confirming the capabilities of PMAp to reproduce the global distribution of aerosol loading. This has been compared to reference sensors such as MODIS and VIIRS. Aerosol optical depth retrieved over ocean and land surfaces is reliable in terms of spatial distribution and temporal variation of the aerosols and their abundance. In addition to AOD, a dedicated PMAp aerosol class is provided in the product. Over land, PMAp is able to identify thick dust or ash. Over water, PMAp can often distinguish between fine and coarse modes, as well as detecting the presence of dust.

The PMAp AOD product has been tested over two time periods, June–September 2013 (validation period 1) and February–May 2015 (validation period 2). For these periods, AOD retrieved from Metop-A and Metop-B observations has been compared against

corresponding ground-based AERONET level 2 data in terms of correlation, bias, offsets, and time patterns. The results of the best fits over ocean and land are reported (e.g., typical correlation from 0.6 to 0.85 with an RMSE close to 0.15/0.20 over ocean/land (for filtered data)).

This paper reported a first-level validation that demonstrates the ability of PMAp to retrieve relevant AOD with a very good spatial and temporal behavior and an acceptable overall performance. A more exhaustive validation is needed and should better document the detailed performance. This ongoing activity will document various aspects, such as the influence of the acquisition geometry and the aerosol model as described in Fougnie et al. [69] or how the performance varies with the surface type. The consistency between the three Metops is also important to document, especially for the most recent Metop-C, which is now becoming fully mature in term of radiometric correction. A more consolidated comparison to MODIS, VIIRS, or Sentinel-3/SLSTR will complement the previous comparisons. Additional validation through model-based comparison can also be provided as documented in Metzger et al. [70].

PMAp AOD is disseminated in near-real-time [28] and is fully operational over the ocean and demonstrational over land (where the retrieval is more challenging and under consolidation). AOD over the ocean has been assimilated by the Copernicus Atmospheric Monitoring System (CAMS) since 2014, in addition to the MODIS AOD [35,71]. This aerosol product is a very good demonstration of the synergistic use of different sensors sharing the same platform Metop. Some possible improvements have already been identified and may be implemented in the near future. This synergistic concept has already been applied to the sensors of the Metop Second Generation platforms (the multidirectional polarimeter 3MI, the spectrometer Sentinel-5, the spectral imager MET-image, and the thermal infrared sounder IASI-NG), which will allow the retrieval of a much-improved suite of aerosol parameters thanks to the comprehensive information content provided by these instruments.

The last version 2.2, of the PMAp products are distributed near-real-time through the EUMETcast-Europe and EUMETcast-Terrestrial since 6 May 2021 [28,72]. A long-term archiving of all PMAp products, including products generated using previous PMAp versions, is accessible through the EUMETSAT data center [73]. A full reprocessing of the time series, from 2007 to 2019, based on the last version 2.2 presented in this paper, has been generated and will also be released soon [73].

Author Contributions: Conceptualization, R.L., M.G., G.P.; methodology, M.G., G.P., A.C., S.J., A.H., R.L., M.V.-N., R.M., B.F.; software, M.G., G.P., A.H.; validation, M.G., G.P., A.C., S.J., A.H., R.L., M.V.-N., R.M., B.F.; formal analysis, M.G., G.P., A.C., S.J., A.H., R.L., M.V.-N., R.M., B.F.; investigation, M.G., G.P., A.C., S.J., A.H., R.L., M.V.-N., R.M., B.F.; writing—original draft preparation, M.G., G.P., A.C.; writing—review and editing, B.F., S.J., R.M.; supervision, R.L., R.M., B.F. All authors have read and agreed to the published version of the manuscript.

Funding: This research received no external funding.

Institutional Review Board Statement: Not applicable.

Informed Consent Statement: Not applicable.

Data Availability Statement: PMAp data can be found in the EUMETSAT data centre (<https://www.eumetsat.int/eumetsat-data-centre> accessed on 14 December 2021), AERONET data can be found in the AERONET NASA server (<https://aeronet.gsfc.nasa.gov/> accessed on 14 December 2021). The MODIS and VIIRS aerosol product can be found in the MODIS NASA web page (<https://modis.gsfc.nasa.gov/data/dataproduct/mod04.php> accessed on 14 December 2021) and in the NASA LAADS DAAC (<https://ladsweb.modaps.eosdis.nasa.gov/missions-and-measurements/products/> accessed on 14 December 2021).

Conflicts of Interest: The authors declare no conflict of interest.

References

1. Boucher, O.; Randall, D.; Artaxo, P.; Bretherton, C.; Feingold, G.; Forster, P.; Kerminen, V.-M.; Kondo, Y.; Liao, H.; Lohmann, U.; et al. Clouds and Aerosols. In *Climate Change 2013: The Physical Science Basis. Contribution of Working Group I to the Fifth Assessment Report of the Intergovernmental Panel on Climate Change*; Stocker, T.F., Qin, D., Plattner, G.-K., Tignor, M., Allen, S.K., Boschung, J., Nauels, A., Xia, Y., Bex, V., Midgley, P.M., Eds.; Cambridge University Press: Cambridge, UK; New York, NY, USA, 2013.
2. Fuzzi, S.; Baltensperger, U.; Carslaw, K.; Decesari, S.; van der Gon, H.D.; Facchini, M.C.; Fowler, D.; Koren, I.; Langford, B.; Lohmann, U.; et al. Particulate matter, air quality and climate: Lessons learned and future needs. *Atmos. Chem. Phys.* **2015**, *15*, 8217–8299. [[CrossRef](#)]
3. Benedetti, A.; Morcrette, J.J.; Boucher, O.; Dethof, A.; Engelen, R.J.; Fisher, M.; Flentje, H.; Huneeus, N.; Jones, L.; Kaiser, J.W.; et al. Aerosol analysis and forecast in the European Centre for Medium Range Weather Forecasts Integrated Forecast System: 2. Data assimilation. *J. Geophys. Res.* **2009**, *114*, D13205. [[CrossRef](#)]
4. Xian, P.; Reid, J.S.; Hyer, E.J.; Sampson, C.R.; Rubin, J.I.; Ades, M.; Asencio, N.; Basart, S.; Benedetti, A.; Bhattacharjee, P.S.; et al. Current state of the global operational aerosol multi-model ensemble: An update from the International Cooperative for Aerosol Prediction (ICAP). *Q.J.R. Meteorol. Soc.* **2019**, *145*, 176–209. [[CrossRef](#)] [[PubMed](#)]
5. Hasekamp, O.P.; Litvinov, P.; Butz, A. Aerosol properties over the ocean from PARASOL multiangle photopolarimetric measurements. *J. Geophys. Res. Space Phys.* **2011**, *116*, D14204. [[CrossRef](#)]
6. Mishchenko, M.; Travis, L.D. Satellite retrieval of aerosol properties over the ocean using polarization as well as intensity of reflected sunlight. *J. Geophys. Res. Space Phys.* **1997**, *102*, 16989–17013. [[CrossRef](#)]
7. Deschamps, P.-Y.; Breon, F.-M.; Leroy, M.; Podaire, A.; Bricaud, A.; Buriez, J.-C.; Seze, G. The POLDER mission: Instrument characteristics and scientific objectives. *IEEE Trans. Geosci. Remote Sens.* **1994**, *32*, 598–615. [[CrossRef](#)]
8. Deuzé, J.L.; Goloub, P.; Herman, M.; Marchand, A.; Perry, G.; Susana, S.; Tanré, D. Estimate of the aerosol properties over the ocean with POLDER. *J. Geophys. Res.* **2000**, *105*, 15329–15346. [[CrossRef](#)]
9. Tanré, D.; Bréon, F.M.; Deuzé, J.L.; Dubovik, O.; Ducos, F.; François, P.; Goloub, P.; Herman, M.; Lifermann, A.; Waquet, F. Remote sensing of aerosols by using polarized, directional and spectral measurements within the A-Train: The PARASOL mission. *Atmospheric Meas. Tech.* **2011**, *4*, 1383–1395. [[CrossRef](#)]
10. Dubovik, O.; Herman, M.; Holdak, A.; Lapyonok, T.; Tanré, D.; Deuzé, J.L.; Ducos, F.; Sinyuk, A.; Lopatin, A. Statistically optimized inversion algorithm for enhanced retrieval of aerosol properties from spectral multi-angle polarimetric satellite observations. *Atmos. Meas. Tech.* **2011**, *4*, 975–1018. [[CrossRef](#)]
11. Torres, B.; Dubovik, O.; Fuertes, D.; Schuster, G.; Cachorro, V.E.; Lapyonok, T.; Goloub, P.; Blarel, L.; Barreto, A.; Mallet, M.; et al. Advanced characterization of aerosol properties from measurements of spectral optical depth using the GRASP algorithm. *Atmos. Meas. Tech.* **2017**, *10*, 3743–3781. [[CrossRef](#)]
12. North, P. Estimation of aerosol opacity and land surface bidirectional reflectance from ATSR-2 dual-angle imagery: Operational method and validation. *J. Geophys. Res.* **2002**, *107*, D12. [[CrossRef](#)]
13. Popp, T.; de Leeuw, G.; Bingen, C.; Bruehl, C.; Capelle, V.; Chedin, A.; Clarisse, L.; Dubovik, O.; Grainiger, R.; Griesfeller, J.; et al. Development, Production and Evaluation of Aerosol Climate Data Records from European Satellite Observations (Aerosol_cci). *Remote Sens.* **2016**, *8*, 421. [[CrossRef](#)]
14. Holzer-Popp, T.; Schroedter-Homscheidt, M.; Breitkreuz, H.; Martynenko, D.; Klueser, L. Improvements of synergetic aerosol retrieval from ENVISAT. *Atmosph. Chem. Phys.* **2008**, *8*, 7651–7672. [[CrossRef](#)]
15. Chimot, J. EUMETSAT Web Site. 2020. Available online: <https://www.eumetsat.int/S3-AOD> (accessed on 1 August 2020).
16. Remer, L.A.; Kaufman, Y.L.; Tanre, D.; Mattoo, S.; Chu, D.A.; Martins, J.V.; Li, R.R.; Ichoku, C.; Levy, R.C.; Kleidman, R.G.; et al. The MODIS aerosol algorithm, products and validation. *J. Atmos. Sci.* **2005**, *62*, 947–973. [[CrossRef](#)]
17. Seidel, F.C.; Popp, C. Critical surface albedo and its implications to aerosol remote sensing. *Atmosph. Meas. Tech.* **2012**, *5*, 1653–1665. [[CrossRef](#)]
18. Hsu, N.C.; Tsay, S.-C.; King, M.D.; and Herman, J.R. Aerosol properties over bright-reflecting source regions. *IEEE Trans. Geosci. Remote Sens.* **2004**, *42*, 557–569. [[CrossRef](#)]
19. Hsu, N.C.; Jeong, M.J.; Bettenhausen, C.; Sayer, A.M.; Hansell, R.; Seftor, C.S.; Huang, J.; Tsay, C.S. Enhanced Deep Blue aerosol retrieval algorithm: The second generation. *J. Geophys. Res.* **2013**, *118*, 1–20. [[CrossRef](#)]
20. Levy, R.C.; Mattoo, S.; Munchak, L.A.; Remer, L.A.; Sayer, A.M.; Patadia, F.; Hsu, N.C. The Collection 6 MODIS aerosol products over land and ocean. *Atmosph. Meas. Tech.* **2013**, *6*, 2989–3034. [[CrossRef](#)]
21. Lyapustin, A.; Wang, Y.; Korkin, S.; Huang, D. MODIS Collection 6 MAIAC algorithm. *Atmos. Meas. Tech.* **2018**, *11*, 5741–5765. [[CrossRef](#)]
22. Sogacheva, L.; Popp, T.; Sayer, A.M.; Dubovik, O.; Garay, M.J.; Heckel, A.; Hsu, N.C.; Jethva, H.; Kahn, R.A.; Kolmonen, P.; et al. Merging regional and global aerosol optical depth records from major available satellite products. *Atmos. Chem. Phys.* **2020**, *20*, 2031–2056. [[CrossRef](#)]
23. Stap, F.A.; Hasekamp, O.P.; Röckmann, T. Sensitivity of PARASOL multi-angle photopolarimetric aerosol retrievals to cloud contamination. *Atmos. Meas. Tech.* **2015**, *8*, 1287–1301. [[CrossRef](#)]
24. Waquet, F.; Peers, F.; Ducos, F.; Goloub, P.; Platnick, S.; Riedi, J.; Tanré, D.; Thieuleux, F. Global analysis of aerosol properties above clouds. *Geophys. Res. Lett.* **2013**, *40*, 5809–5814. [[CrossRef](#)]

25. Clarisse, L.; Coheur, P.F.; Prata, F.; Hadji-Lazaro, J.; Hurtmans, D.; Clerbaux, C. A unified approach to infrared aerosol remote sensing and type specification. *Atmosph. Chem Phys.* **2013**, *13*, 2195–2221. [[CrossRef](#)]
26. Klaes, D.; Cohen, M.; Buhler, Y.; Schlüssel, P.; Munro, R.; Luntama, J.P.; von Engeln, A.; O’Clerigh, E.; Bonekamp, H.; Ackermann, J.; et al. An Introduction to the EUMETSAT Polar system. *B. Am. Meteorol. Soc.* **2007**, *88*, 1085–1096. [[CrossRef](#)]
27. EUMETCast Web Page. Available online: <https://www.eumetsat.int/eumetcast> (accessed on 1 August 2020).
28. EUMETSAT, Polar Multi-Sensor Aerosol Product: Validation Report, v4A, EUM/TSS/REP/14/745438, EUMETSAT Web Page. 2021. Available online: <https://www.eumetsat.int/media/40632> (accessed on 1 May 2020).
29. Munro, R.; Lang, R.; Klaes, D.; Poli, G.; Retscher, C.; Lindstrot, R.; Huckler, R.; Lacan, A.; Grzegorski, M.; Holdak, A.; et al. The GOME-2 instrument on the Metop-series of satellites: Instrument design, calibration and level 1 data processing—An overview. *Atmos. Meas. Tech.* **2016**, *9*, 1279–1301. [[CrossRef](#)]
30. Ignatov, A.; Sapper, J.; Cox, S.; Laszlo, I.; Nalli, N.R.; Kidwell, K.B. Operational Aerosol Observations (AEROBS) from AVHRR/3 On Board NOAA-KLM Satellites. *J. Atmospheric Ocean. Technol.* **2004**, *21*, 3–26. [[CrossRef](#)]
31. Hauser, A.; Oesch, D.; Foppa, N.; Wunderle, S. NOAA AVHRR derived aerosol optical depth over land. *J. Geophys. Res.* **2005**, *110*, D08204. [[CrossRef](#)]
32. Hsu, N.C.; Lee, J.; Sayer, A.M.; Carletta, N.; Chen, S.-H.; Tucker, C.J.; Holben, B.N.; Tsay, S.-C. Retrieving near-global aerosol loading over land and ocean from AVHRR. *J. Geophys. Res.* **2017**, *122*, 9968–9989. [[CrossRef](#)]
33. Sayer, A.M.; Hsu, N.C.; Lee, J.; Carletta, N.; Chen, S.-H.; Smirnov, A. Evaluation of NASA Deep Blue/SOAR aerosol retrieval algorithms applied to AVHRR measurements. *J. Geophys. Res. Atmos.* **2017**, *122*, 9945–9967. [[CrossRef](#)]
34. Clerbaux, C.; Boynard, A.; Clarisse, L.; George, M.; Hadji-Lazaro, J.; Herbin, H.; Hurtmans, D.; Pommier, M.; Razavi, A.; Turquety, S.; et al. Monitoring of atmospheric composition using the thermal infrared IASI/Metop sounder. *Atmosph. Chem. Phys.* **2009**, *9*, 6041–6054. [[CrossRef](#)]
35. Inness, A.; Ades, M.; Agustí-Panareda, A.; Barré, J.; Benedictow, A.; Blechschmidt, A.-M.; Dominguez, J.J.; Engelen, R.; Eskes, H.; Flemming, J.; et al. The CAMS reanalysis of atmospheric composition. *Atmos. Chem. Phys.* **2019**, *19*, 3515–3556. [[CrossRef](#)]
36. Schlüssel, P.; Kayal, G. Introduction to the next generation EUMETSAT Polar System (EPS-SG) observation missions. In *Proceedings of the Sensors, Systems, and Next-Generation Satellites XXI*; Neeck, S.P., Bézy, J.-L., Kimura, T., Shimoda, H., Meynart, R., Eds.; SPIE: Warsaw, Poland, 2017; Volume 10423, pp. 1–16.
37. Callies, J.; Corpaccioli, E.; Eisinger, M.; Hahne, A.; Lefebvre, A. GOME-2—Metop’s Second-Generation Sensor for Operational Ozone Monitoring. *ESA Bull. Eur. Space* **2000**, *102*, 28–36.
38. Grzegorski, M.; Wenig, M.; Platt, U.; Stammes, P.; Fournier, N.; Wagner, T. The Heidelberg Iterative Cloud Retrieval Utilities (HICRU) and its application to GOME-2 data. *Atmos. Chem. Phys.* **2006**, *6*, 4461–4476. [[CrossRef](#)]
39. Wang, P.; Stammes, P.; van der A, R.; Pinardi, G.; van Roozendael, M. FRESCO+: An improved O₂ A-band cloud retrieval algorithm for tropospheric trace gas retrievals. *Atmos. Chem. Phys. Discuss.* **2008**, *8*, 6565–6576. [[CrossRef](#)]
40. Jafariserajehlou, S.; Fougne, B. EPS/GOME-2 PMD Radiometric Adjustment over Rayleigh scattering. In *Proceedings of the GSICS Annual Meeting, Virtual Meeting*, 31 March 2021.
41. Cracknell, A.P. *The Advanced Very High Resolution Radiometer (AVHRR)*; Taylor & Francis: London, UK, 1997.
42. NOAA. NOAA-KLM User’s Guide. 2014. Available online: <https://www1.ncdc.noaa.gov/pub/data/satellite/publications/podguides/> (accessed on 25 August 2014).
43. Nagle, F.W.; Holz, R.E. Computationally Efficient Methods of Collocating Satellite, Aircraft, and Ground Observations. *J. Atmos. Oceanic Technol.* **2009**, *26*, 1585–1595. [[CrossRef](#)]
44. Wang, L.; Tremblay, D.; Zhang, B.; Han, Y. Fast and Accurate Colocation of the Visible Infrared Imaging Radiometer Suite Measurements with Cross-Track Infrared Sounder. *Remote Sens.* **2016**, *8*, 76. [[CrossRef](#)]
45. Lang, R.; Poli, G.; Fougne, B.; Lacan, A.; Marbach, T.; Riédi, J.; Schluessel, P.; Couto, A.B.; Munro, R. The 3MI Level-1C Geo-projected Product—Definition and Processing Description. *J. Quant. Spectrosc. Rad. Transf.* **2019**, *225*, 91–109. [[CrossRef](#)]
46. O’Rourke, J. *Computational Geometry in C*, 2nd ed.; Cambridge University Press: Cambridge, UK, 1998; par. 7.6; pp. 252–264.
47. GOME-2 Factsheet, EUMETSAT, EUM/OPS/DOC/10/1299, GOME-2 Web Page. 2015. Available online: <https://www.eumetsat.int/gome-2> (accessed on 27 April 2017).
48. Latter, B.; Lang, R.; Munro, R. Cross—Comparison of GOME-2, AVHRR and AASTR Reflectance. GSICS Quarterly Report, V5, No. 3. 2011. Available online: <http://gsics.wmo.int> (accessed on 14 December 2021).
49. Hasekamp, O.P.; Landgraf, J. Retrieval of aerosol properties over the ocean from multispectral single-viewing-angle measurements of intensity and polarization: Retrieval approach, information content and sensitivity study. *J. Geophys. Res.* **2005**, *110*, D20207. [[CrossRef](#)]
50. Hasekamp, O.P.; Tuinder, O.; Stammes, P. Final Report of the O3M-SAF Activity: Aerosol Retrieval from GOME-2: Improving Computational Efficiency and First Application. 2008. Available online: o3msaf.fmi.fi/docs/vs/2008/Hasekamp_final_report.pdf (accessed on 14 December 2021).
51. Prata, F. Observations of volcanic ash clouds in the 10–12 μm window using AVHRR/2 data. *Int. J. Remote Sens.* **1989**, *10*, 751–761. [[CrossRef](#)]
52. De Graaf, M.; Stammes, P.; Torres, O.; Koelemeijer, R.B.A. Absorbing Aerosol Index: Sensitivity analysis, application to GOME-2 and comparison with TOMS. *J. Geophys. Res.* **2005**, *110*, D010201. [[CrossRef](#)]

53. Clarisse, L.; Hurtmans, D.; Clerbaux, C.; Hadji-Lazaro Ngadi, J.Y.; Coheur, P.F. Retrieval of sulphur dioxide from the infrared atmospheric sounding interferometer (IASI). *Atmos. Meas. Tech.* **2012**, *5*, 581–594. [[CrossRef](#)]
54. Tanré, D.; Herman, M.; Kaufman, Y. Information on the aerosol size distribution contained in the solar reflected spectral radiances. *J. Geophys. Res.* **1996**, *101*, 19043–19060. [[CrossRef](#)]
55. AVHRR Level-1B Product Guide. 2011. Available online: https://www-cdn.eumetsat.int/files/2020-04/pdf_avhrr_l1b_product_guide.pdf (accessed on 21 January 2011).
56. Dybbroe, A.; Karlsson, K.-G.; Thoss, A. NWCSAF AVHRR Cloud Detection and Analysis Using Dynamic Thresholds and Radiative Transfer Modeling. Part I: Algorithm Description. *J. Appl. Met.* **2005**, *44*, 39–54. [[CrossRef](#)]
57. Koelemeijer, R.B.A.; Stammes, P.; Hovenier, J.W.; de Haan, J.F. Global distributions of effective cloud fraction and cloud top pressure derived from oxygen A band spectra measured by the Global Ozone Monitoring Experiment: Comparison to ISCCP data. *J. Geophys. Res.* **2002**, *107*, 4151. [[CrossRef](#)]
58. Smith, W.L.; Platt, C.M.R. Comparison of satellite deduced cloud heights with indications from radiosonde and ground-based lidar measurements. *J. Appl. Met.* **1978**, *17*, 1796–1802. [[CrossRef](#)]
59. Tilstra, L.; Tuinder, O.N.E.; Wang, P.; Stammes, P. Surface reflectivity climatologies from UV to NIR determined from Earth Observations by GOME-2 and SCIAMACHY. *J. Geophys. Res.* **2017**, *122*, 4084–4111. [[CrossRef](#)]
60. Popp, C.; Wang, P.; Brunner, D.; Stammes, P.; Zhou, Y.; Grzegorski, M. MERIS albedo climatology for FRESCO O2-A-band cloud retrieval. *Atmos. Meas. Tech.* **2011**, *4*, 463–483. [[CrossRef](#)]
61. Clarisse, L.; Prata, F.; Lacour, J.L.; Hurtmans, D.; Clerbaux, C.; Coheur, P.F. A correlation method for volcanic ash detection using hyperspectral infrared measurements. *Geophys. Res. Lett.* **2010**, *37*, L19806. [[CrossRef](#)]
62. Sayer, A.M.; Hsu, N.C.; Bettenhausen, C.; Lee, J.; Kim, W.V.; Smirnov, A. Satellite Ocean Aerosol Retrieval (SOAR) Algorithm Extension to S-NPP VIIRS as Part of the “Deep Blue” Aerosol Project. *J. Geophys. Res. Atmos.* **2018**, *123*, 380–400. [[CrossRef](#)] [[PubMed](#)]
63. Levy, R.C.; Remer, L.A.; Mattoo, S.; Vermote, E.F.; Kaufman, Y.J. Second-generation operational algorithm: Retrieval of aerosol properties over land from inversion of Moderate Resolution Imaging Spectroradiometer spectral reflectance. *J. Geophys. Res.* **2007**, *112*, D13211. [[CrossRef](#)]
64. CAMS. How Wildfires in the Americas and Tropical Africa in 2020 Compared to Previous Years. 2020. Available online: <https://atmosphere.copernicus.eu/how-wildfires-americas-and-tropical-africa-2020-compared-previous-years> (accessed on 14 December 2020).
65. Wang, X.; Cheng, H.; Che, H.; Sun, J.; Lu, H.; Qiang, M.; Hua, T.; Zhu, B.; Li, H.; Ma, W.; et al. Modern dust aerosol availability in northwestern China. *Sci. Rep.* **2017**, *7*, 1–8. [[CrossRef](#)]
66. Santoso, M.; Lestiani, D.D.; Kurniawati, S.; Damastuti, E.; Kusmartini, I.; Atmodjo, D.P.D.; Sari, D.K.; Hopke, P.K.; Mukhtar, R.; Muhtarom, T.; et al. Assessment of Urban Air Quality in Indonesia. *Aerosol Air Qual. Res.* **2020**, *20*, 2142–2158. [[CrossRef](#)]
67. Holben, B.N.; Eck, T.F.; Slutsker, I.; Tanré, D.; Buis, J.P.; Setzer, A.; Vermote, E.; Reagan, J.A.; Kaufman, Y.J.; Nakajima, T.; et al. AERONET A Federated Instrument Network and Data Archive for Aerosol Characterization. *Remote Sens. Environ.* **1998**, *66*, 1–16. [[CrossRef](#)]
68. MODIS Climatology, Earth Observatory NASA Web Site. Available online: https://earthobservatory.nasa.gov/global-maps/MODAL2_M_AER_OD (accessed on 1 August 2020).
69. Fougnie, B.; Chimot, J.; Vazquez-Navarro, M.; Marbach, T.; Bojkov, B. Aerosol Retrieval from Space—How the Geometry of Acquisition Impacts our Ability to Characterize Aerosol Properties. *J. Quant. Spectr. Rad. Transf.* **2020**, *256*, 1–12. [[CrossRef](#)]
70. Metzger, S.; Abdelkader, M.; Klingmüller, K.; Steil, B.; Cacciari, A.; Grzegorski, M.; Lang, R.; Munro, R.; Vazquez-Navarro, M.; Fougnie, B. Evaluation of the MetOp PMAp version 2 AOD products using EMAC model data, AERONET ground station and reference satellite observations (MISR and MODIS-Aqua/Terra). *Atmosph. Chem. Phys.* **2021**. (in prep.)
71. Benedetti, A.; Di Giuseppe, F.; Jones, L.; Peuch, V.-H.; Rémy, S.; Zhang, X. The value of satellite observations in the analysis and short-range prediction of Asian dust. *Atmos. Chem. Phys.* **2019**, *19*, 987–998. [[CrossRef](#)]
72. EUMETSAT—Product Navigator—Polar Multi-Sensor Aerosol Optical Properties—Metop. Available online: <https://navigator.eumetsat.int/product/EO:EUM:DAT:METOP:PMAP> (accessed on 28 February 2014).
73. EUMETSAT Data Centre/EUMETSAT. Available online: <https://www.eumetsat.int/eumetsat-data-centre> (accessed on 1 August 2020).